Thesis for the degree of Philosophiae Doctor

Currents and mean circulation induced by trapped internal waves

Eivind Støylen

Meteorology and Oceanography Section

Department of Geosciences

Faculty of Mathematics and Natural Sciences

University of Oslo

Series of dissertations submitted to the
Faculty of Mathematics and Natural Sciences, University of Oslo
No. 1314

ISSN 1501-7710

Cover: Inger Sandved Anfinsen.
Printed in Norway: AIT Oslo AS.

Produced in co-operation with Akademika publishing.
The thesis is produced by Akademika publishing merely in connection with the thesis defence. Kindly direct all inquiries regarding the thesis to the copyright holder or the unit which grants the doctorate.

Preface

The present thesis is entitled "Currents and mean circulation induced by trapped internal waves", and is based on the following three papers:

I. Støylen, E., and J. E. H. Weber (2010), Mass transport induced by internal Kelvin waves beneath shore-fast ice, *J. Geophys. Res., 115,* C03022, doi:10.1029/2009JC005298

II. Weber, J. E. H., and E. Støylen (2011), Mean drift velocity in the Stokes interfacial edge wave, *J. Geophys. Res., 116,* C04002, doi:10.1029/2010JC006619

III. Støylen, E. (2012), Tidally induced internal motion in an Arctic fjord, *Manuscript in preparation*

First and foremost I must thank my principal supervisor, Prof. Jan Erik Weber. He introduced me to the very interesting concept of wave-induced drift in internal Kelvin waves, and has been a pillar of support and contribution through all these years. Secondly, I would like to thank my subsidiary supervisor Prof. Joseph Henry LaCasce, as well as Dr. Göran Broström and Dr. Pål Erik Isachsen for valuable discussions and input. I would also like to thank friends and collegues at the MetOs section for a great working environment, academically and socially.

And of course, to my wife Karen who gave birth to my son Oskar just when I was finishing this work. Your continuous patience and understanding is invaluable.

November, 2012

An introductory overview

1. Introduction

Internal waves in the ocean may exist wherever there is vertical stratification. They are generated by disturbance of the water column, typically when the barotropic tide interacts with topography, or from changes in the wind. The scales range from several hours to a few minutes or seconds, and amplitudes in the order of tens of meters are common [*Garrett and Munk*, 1979]. The literature on internal waves is ever growing; see e.g. *Vlasenko et al.* [2005] for a list of relevant work.

In the present thesis we consider trapped internal waves. Two classes of trapped waves are examined; the internal Kelvin wave (papers I and III) trapped by the Coriolis force, and the Stokes interfacial edge wave (paper II) which is trapped due to a sloping bottom. In particular we explore the non-linear wave-induced drift inherent in these waves. When waves propagate along topography, a mean current is induced in the direction of wave propagation. The associated mean mass transport will systematically relocate water which may lead to accumulation or deposition of pollutants, oil spill, and biological material in certain areas along the bottom slope or coastline. Our aim is to quantify this transport in idealized geometries, and relate the results to the real world.

Regarding the internal Kelvin wave, one particular application of interest is the Arctic region. In later years this region has received increased attention with respect to ship traffic, oil drilling, fishery and climate change. In paper I we develop an idealized theory concerning wave drift in internal Kelvin waves beneath shore fast ice. There are several locations in the Arctic where this theory may be valid, for instance the Barents Sea, Baffin Bay or several of

the wide (with respect to the baroclinic Rossby radius) fjords along the Arctic coastline. One example of such an Arctic fjord is Van Mijenfjorden in Svalbard [*Skarðhamar and Svendsen*, 2010]. This fjord is studied more closely in paper III. We consider an ice-free summer scenario, and employ a numerical model and measurements in an attempt to verify the presence of internal Kelvin waves in this fjord. These waves would in turn induce a mean current propagating cyclonically around the basin.

In the next subsection some background and explanation on the wave-drift concept is given, followed by a discussion on numerical treatment of internal waves. A summary of papers is given in section 2, and concluding marks in section 3.

1.1 On wave- induced currents

The principle of wave-induced drift stems from the original theory of *Stokes* [1847], who considered waves propagating in an inviscid fluid. He showed that the trajectory of individual fluid particles under a propagating wave form nearly closed ellipsis, but when averaging over a wave period the particles are in fact displaced a small distance in the direction of wave propagation. *Longuet-Higgins* [1953] extended the analysis to viscous fluids. The basis of his derivations is briefly presented in the following.

Consider periodic horizontal wave motion $\boldsymbol{u}_e(\boldsymbol{x}, t)$ in an Eulerian framework (*x,y,z*). For a fluid particle situated at $\boldsymbol{x} = \boldsymbol{a}$ at time $t = t_0$, its displacement at time t may be expressed as $\boldsymbol{x} = \boldsymbol{a} + \int_{t_0}^{t} \boldsymbol{u}_l(\boldsymbol{a}, t')dt'$, where $\boldsymbol{u}_l$ is the Lagrangian velocity of the particle. The relation between $\boldsymbol{u}_l$ and $\boldsymbol{u}_e$ when considering small displacements is

$$\boldsymbol{u}_l(\boldsymbol{a},t) = \boldsymbol{u}_e(\boldsymbol{x},t) = \boldsymbol{u}_e\left(\boldsymbol{a} + \int_{t_0}^{t} \boldsymbol{u}_l(\boldsymbol{a},t')dt', t\right)$$
$$= \boldsymbol{u}_e(\boldsymbol{a},t) + \left(\int_{t_0}^{t} \boldsymbol{u}_l(\boldsymbol{a},t')dt'\right)\cdot\nabla_a\boldsymbol{u}_e(\boldsymbol{a},t) + \mathcal{O}(\varepsilon^3)\,, \tag{1}$$

by use of Taylor's theorem. Here we have expanded the variables as $\boldsymbol{u} = \widetilde{\boldsymbol{u}}\varepsilon + \overline{\boldsymbol{u}}\varepsilon^2 + \boldsymbol{u}_3\varepsilon^3$ ... for a small parameter ε. From (1) it is evident that $\boldsymbol{u}_l(\boldsymbol{a},t)$ and $\boldsymbol{u}_e(\boldsymbol{a},t)$ are equal to the first order in ε. The balance to the second order is obtained by averaging (1) over a wave period, denoted by an over-bar, assuming that $\overline{(\widetilde{\boldsymbol{u}})} = 0$:

$$\overline{\boldsymbol{u}}_l(\boldsymbol{a},t) = \overline{\boldsymbol{u}}_e(\boldsymbol{a},t) + \overline{\left(\int_{t_0}^{t} \widetilde{\boldsymbol{u}}_l(\boldsymbol{a},t')dt'\right)\cdot\nabla_a\widetilde{\boldsymbol{u}}_e(\boldsymbol{a},t)} = \overline{\boldsymbol{u}}_e(\boldsymbol{a},t) + \overline{\boldsymbol{u}}_s(\boldsymbol{a},t). \tag{2}$$

The total second order mean wave induced flow consists of two terms; the Stokes drift $\overline{\boldsymbol{u}}_s(\boldsymbol{a},t)$, and a mean Eulerian drift term $\overline{\boldsymbol{u}}_e(\boldsymbol{a},t)$.

As discussed in *Longuet-Higgins* [1953], $\overline{\boldsymbol{u}}_e$ is not necessarily zero. Considering non-rotating propagating surface waves in a tank, he observed that the presence of viscosity induces a new drift term near the rigid bottom in the direction of wave propagation. After this momentum has diffused through the fluid, the resulting vertically integrated volume flux $\overline{\boldsymbol{U}}_e$ is actually 3/2 times the Stokes flux for shallow water waves. In papers I and II we do a similar comparison for the case of internal Kelvin waves and interfacial Stokes edge waves respectively. In accordance with Longuet-Higgins' experiment, we utilize rigid boundaries (i.e. surface ice and sloping bottom) onto which no-slip boundary conditions are imposed, providing the dominant friction in the system. The resulting Eulerian fluxes are shown to relate to the respective Stokes fluxes in quite comparable ways to the surface shallow water case.

Wave-induced drift is inherently of a Lagrangian nature; thus it is physically intuitive to utilize Lagrangian coordinates in the calculations, as shown numerous times in literature [e.g. *Ünlüata and Mei*, 1970; *Weber*, 1983; *Jenkins*, 1987]. In this thesis however we are primarily interested in the mean transport. Thus we utilize the Eulerian approach, and encompass the Lagrangian transport property by integrating the momentum and continuity equations in the vertical between material surfaces as described in *Phillips* [1977]. In fact, we solve two sets of equations. First we solve for the linear first order motion by conventional Eulerian approach. From the first order solution the Stokes drift is obtained, which after integration may be subtracted from the vertically integrated Lagrangian fluxes in order to obtain equations for $\overline{\boldsymbol{U}}_e$.

1.2 Numerical treatment of internal waves

In all numerical modeling problems there is a natural restriction in available computational resources. Consequently one must take care when designing numerical experiments. For internal waves in the ocean, this means to be aware what waves and processes one wants to resolve. Propagation of large scale linear waves demands far less computational resources than for instance generation processes near sills, nonlinear steepening of wave fronts and wave breaking. Besides, the scale of topographic features demands sufficient resolution to be properly represented.

Various methods have been utilized to remedy the computational restrictions. In early days a common approach was to use a two-layer system [i.e. *O'Brien and Hurlburt*, 1972; *Hurlburt and Thompson*, 1980] solving for the interface and free surface. This is in fact a surprisingly robust method for laminar flow and is in use for higher horizontal resolutions also today [*Brandt et al.*, 2004]. Another common approach is to consider only one horizontal

dimension in addition to the vertical. This allows very high resolution which is a requirement when considering non-hydrostatic processes; i.e. Δx must be less than the typical pycnocline depth [*Vitousek and Fringer*, 2011]. Examples of such processes are internal wave breaking at topographic slopes [*Vlasenko and Hutter*, 2002; *Legg and Adcroft*, 2003] and mixing processes and wave generation near sills [*Davies and Xing*, 2007; *Xing and Davies*, 2009].

For basin scale internal waves, *Hodges et al.* [2000] managed to successfully simulate the internal Kelvin wave induced by wind using a course-resolution ($\Delta x = 400$ m) hydrostatic model. Recently non-hydrostatic simulations in three dimensions has become possible for high resolutions ($\Delta x = 20$m), as demonstrated by *Boegman and Dorostkar* [2011] simulating nonlinear internal waves in a 62*3 km lake. For our simulations presented in paper III the main goal is to simulate internal Kelvin waves in a rather large fjord (50*10 km) generated at narrow sounds. Thus our problem involves two different spatial scales; the wave generation area and the larger scale wave propagating around the basin. Due to the fjord width it is not really computationally reasonable to apply high resolutions in the entire fjord. At the same time we need to properly resolve the wave generation which demands rather higher resolutions than the wind induced generation mechanisms of Hodges et al. As will be seen we choose to apply middle-of-the-road resolutions ($\Delta x = 100$ m) in the entire basin.

2. Summary of papers

2.1: Støylen, E., and J. E. H. Weber (2010); Mass transport induced by internal Kelvin waves beneath shore-fast ice

Here we consider the internal Kelvin wave in an idealized one-layer reduced gravity model beneath an ice lid. By integrating in the vertical between material boundaries we obtain equations by which the wave averaged mass transport is calculated. Non-linear wave forcing

terms enter these equations similar to the radiation stress terms of *Longuet-Higgins and Stewart* [1962]. As discussed in section 1.1, the mean transport consists of two terms; the Stokes drift and the Eulerian mean drift emerging due to friction. We separate the effect of friction on the wave motion and the mean flow. For the linear wave we impose a no-slip condition under the ice, whereas for the mean flow we utilize a drag formalism taking the stress components to be proportional to the square of the mean Eulerian velocities.

We take horizontal coordinates *x,y* where land is at $y<0$. The resulting linear wave motion ξ along the interface is $\xi = A\, e^{-\alpha x - y/a} e^{i\psi}$ where α is a friction coefficient, a is the internal Rossby radius and ψ is the phase function. The Stokes drift term $\overline{U}_S$ is shown to be proportional to $e^{-2(\alpha x + y/a)}$ and the mean Eulerian drift $\overline{U}_E$ goes as $e^{-\alpha x - y/a}$. When inserting appropriate values for the relevant physical parameters we get $\overline{U}_E = 2.2\, \overline{U}_S$ near the coast, which is in good agreement with Longuet-Higgins' result for shallow water shown in section 1.1.

Due to the horizontal divergence of the mean flow, an outward drift component normal to the coast is induced. Motivated by this result, we perform a simple two-dimensional numerical simulation on the mean flow in confined basins. The result shows that for sufficient wave amplitudes, the mean drift is indeed propagating around the basin as one would expect. Due to the cross-coast outward flow, the associated thinning of the near-coast upper layer induces a geostrophically balanced return flow just outside the trapping region of the internal Kelvin wave. This particular theoretical concept can, however interesting, not be expected to be of much significance in the real world. We do however argue that the along-shore mean transport is of importance in the numerous regions with significant internal Kelvin wave activity. In ice-free regions the Eulerian drift is weaker due to reduced friction; however it will still be present due to turbulent friction between the layers. Besides, the Stokes drift is

unaltered so the mean induced drift is relevant also in summer conditions and in stratified non-Arctic environments.

2.2: Weber, J. E. H., and E. Støylen (2011); Mean drift velocity in the Stokes interfacial edge wave

In this paper we look at the Stokes interfacial edge wave, and apply an analysis similar to that of paper I. We consider an upside-down reduced gravity model, with a thin bottom layer beneath a very thick upper layer. The bottom is sloping linearly downwards in the positive *x*-direction, providing the necessary condition for propagating Stokes edge waves along the interface. Such waves may exist in bottom pools of dense bottom water in the ocean where the interface intersects the continental slope, for instance in the Denmark Strait [*Smith*, 1976].

We take no-slip condition at the bottom, and consider waves with frequency ω larger than the Coriolis parameter *f*. The resulting interfacial wave may propagate in both positive ($\alpha > 0$) and negative ($\alpha < 0$) *y*-direction; the resulting linear wave field is

$$\xi = \xi_0 \exp(-kx - \alpha y)\cos(-\alpha x + ky - \omega t)\ , \qquad (3)$$

where α is a friction coefficient and k,ω are wave number and frequency, respectively. Similar to the internal Kelvin wave, the effect of friction is to dampen the wave amplitude along-shore, in addition to tilting the co-phase lines with respect to the *x*-axis.

By integrating the momentum equations between material surfaces we obtain equations for the mean wave induced drift, here using a linear friction term. Solutions are attained using exponential integrals and numerical evaluation. The resulting non-dimensionalized mean drift velocity q_L consist of a Stokes drift (q_S) and an Eulerian drift (q_E) component as before. An example is shown in the figure on the right from page 6 in the paper

for a particular choice of physical parameters relevant to forcing from the semi-diurnal tide. Near X=0 the Eulerian drift is dominating the Stokes drift. Further seaward q_E actually becomes negative, which restricts the total Lagrangian transport to a rather narrow wedge near X=0. Many of the qualitative features are retained when considering shorter wavelengths.

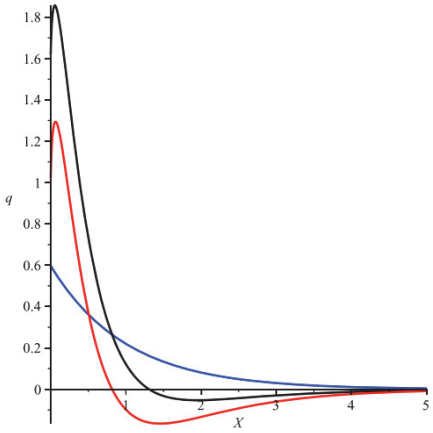

Figure 2. Nondimensional mean velocity q as function of nondimensional seaward distance X for interfacial edge waves with λ = 60 km (period 12.3 h). Blue curve indicates Stokes drift velocity q_S, red curve indicates Eulerian mean current q_E, and black curve indicates Lagrangian mean drift current q_L.

The second order wave forcing terms in the mean equations are shown to be $-\partial E/\partial y$ (for the y-component) where E is wave energy density. This result is between the deep- and shallow water values of *Longuet-Higgins and Stewart* [1960] in a non-rotating ocean, i.e. $-\frac{1}{2}\partial E/\partial y$ and $-\frac{3}{2}\partial E/\partial y$ respectively. This is due to the along-slope current component present in edge waves. A parallel is drawn to surface Poincaré waves over a flat bottom. There rotation induces oscillation in the cross-wave direction, and the resulting wave forcing term is less than $\frac{3}{2}\partial E/\partial y$ due to the Coriolis term.

2.3: Støylen, E. (2012); Tidally induced internal motion in an Arctic fjord

Motivated by the findings in paper I, it is of interest to look more closely at the internal Kelvin wave in an Arctic fjord. We take Van Mijenfjorden in Svalbard as our example. The goal is to describe the tidally induced internal wave pattern through measurements and numerical simulations, and hopefully learn something about how the wave field here may relate to wave induced drift in an idealized basin. As the entrance of Van Mijenfjorden

consists of two sounds, we take the opportunity to investigate the response of two potential wave generators in the basin.

CTD-sections and time series are conducted during August 2010. During this period the fjord is ice free, and the water is well stratified supporting the presence of internal waves. 13-hour time series are taken near the coast around the basin. Comparing the measurements at opposite sides of the fjord, the difference in baroclinic activity clearly suggests internal waves of Kelvin-type. From the data near the fjord entrance, there is indication of a hydraulic jump and associated super-critical motion with respect to the baroclinic phase velocity. A discussion on generation of internal waves in so-called "jet-basins" is given in the paper.

For the numerical part of this study we utilize a non-linear three-dimensional numerical model, namely the MIT general circulation model (MITgcm). As our primary interest is the internal Kelvin wave, we consider only forcing by tides through an open boundary, and set the initial hydrography to only vary in the vertical. Several topographies are considered; first an idealized box with one sound, then Van Mijenfjorden with both sounds open, then we close each sound respectively. In the box we vary the forcing amplitude, in order to test the response when the velocity through the sound is sub-, or supercritical with respect to the baroclinic phase velocity.

From the model runs we clearly see an internal Kelvin signal for all topographies, and for both super- and subcritical conditions. Accordingly we believe that systematic wave-induced transport is relevant in Van Mijenfjorden during summer stratification. Due to our hydrostatic assumption and somewhat crude horizontal resolution (100m grid size), non-physical secondary wave features emerged in the model results. These shortcomings and their consequence are discussed in the paper.

3. Concluding remarks

Through the three papers presented in this thesis we have taken careful steps in the direction of understanding processes related to mass transport induced by trapped internal waves. The waves under consideration have wavelengths of order kilometers and periods of order hours, and may propagate systematically in one direction for a large amount of time. The mean drift velocity is not easily observed by stationary current meters, in part due to the nature of the Stokes drift, but also due to the small amplitudes. It is only after a long period of time we may expect any systematic results with respect to relocation of pollutants, larvae or other passive tracers. It is our belief however that knowledge of these effects is of importance. To our knowledge the results reported here are novel in the literature, and thus this thesis and the respective papers serve as a supplement.

Moving forward there are several steps one can take in order to improve our understanding of the wave drift. For Rossby waves, SOFAR float data has been used to calculate the wave induced drift [*Price and Rossby*, 1982; *LaCasce*, 2008]. Similar methods could be applied in regions of strong internal Kelvin wave activity. Such studies have not yet been performed to the author's knowledge. Further, it would be of interest to address the problem experimentally in a stratified rotating tank. By adding and removing a surface film one might be able to relate the associated change in mean wave drift to the effect of an ice cover on wave drift in the ocean. Finally, more extensive numerical work would be quite fruitful. Given sufficient computational resources one could conduct three-dimensional simulations of sufficient resolution as to accurately describe the wave generation process. Thus a more realistic wave field would be obtained, and a Lagrangian analysis could be performed on the model output to extract the particle drift in the resulting wave. In our case (i.e. paper III) the setup was of a more experimental nature, and computation of the wave induced drift was outside our scope.

References

Boegman, L., and A. Dorostkar (2011), Three-dimensional simulation of NLIW generation, propagation and breaking in Cayuga Lake, in *7th Int. Symp. on Stratified Flows*, edited, Rome, Italy.

Brandt, P., A. Rubino, D. V. Sein, B. Baschek, A. Izquierdo, and J. O. Backhaus (2004), Sea Level Variations in the Western Mediterranean Studied by a Numerical Tidal Model of the Strait of Gibraltar, *J. Phys. Oceanogr.*, *34*(2), 433-443.

Davies, A. M., and J. Xing (2007), On the influence of stratification and tidal forcing upon mixing in sill regions, *Ocean Dynamics*, *57*, 431-451.

Garrett, C., and W. Munk (1979), Internal Waves in the Ocean, *Annual Review of Fluid Mechanics*, *11*(1), 339-369.

Hodges, B. R., J. Imberger, A. Saggio, and K. B. Winters (2000), Modeling basin-scale internal waves in a stratified lake, *Limnol. Oceanogr.*, *45*, 1603-1620.

Hurlburt, H. E., and J. D. Thompson (1980), A Numerical Study of Loop Current Intrusions and Eddy Shedding, *J. Phys. Oceanogr.*, *10*(10), 1611-1651.

Jenkins, A. D. (1987), Wind and Wave Induced Currents in a Rotating Sea with Depth-varying Eddy Viscosity, *J. Phys. Oceanogr.*, *17*(7), 938-951.

LaCasce, J. H. (2008), Statistics from Lagrangian observations, *Prog. Oceanogr.*, *77*(1), 1-29.

Legg, S., and A. Adcroft (2003), Internal Wave Breaking at Concave and Convex Continental Slopes*, *J. Phys. Oceanogr.*, *33*(11), 2224-2246.

Longuet-Higgins, M. S. (1953), Mass transport in water waves, *Philos. Trans. R. Soc. London*, *245A*(903), 535-581.

Longuet-Higgins, M. S., and R. W. Stewart (1960), Changes in the form of short gravity waves on long waves and tidal currents, *J. Fluid Mech.*, *8*(04), 565-583.

Longuet-Higgins, M. S., and R. W. Stewart (1962), Radiation stress and mass transport in gravity waves, with application to 'surf-beats', *J. Fluid Mech.*, *13*(4), 481-504.

O'Brien, J. J., and H. E. Hurlburt (1972), A Numerical Model of Coastal Upwelling, *J. Phys. Oceanogr.*, *2*(1), 14-26.

Phillips, O. M. (1977), *The Dynamics of the Upper Ocean*, 2 ed., Cambridge University Press, New York.

Price, J. F., and T. Rossby (1982), Observations of a barotropic planetary wave in the western North Atlantic, *J. Mar. Res.*, *40*, 543-558.

Skarðhamar, J., and H. Svendsen (2010), Short-term hydrographic variability in a stratified Arctic fjord, *Geological Society, London, Special Publications*, *344*(1), 51-60.

Smith, P. C. (1976), Baroclinic Instability in the Denmark Strait Overflow, *J. Phys. Oceanogr.*, *6*(3), 355-371.

Stokes, G. G. (1847), On the theory of oscillatory waves, *Trans. Camb. Phil. Soc*.

Vitousek, S., and O. B. Fringer (2011), Physical vs. numerical dispersion in nonhydrostatic ocean modeling, *Ocean Modelling*, *40*(1), 72-86.

Vlasenko, V., and K. Hutter (2002), Numerical Experiments on the Breaking of Solitary Internal Wavesover a Slope–Shelf Topography, *J. Phys. Oceanogr.*, *32*(6), 1779-1793.

Vlasenko, V., N. Stashchuk, and K. Hutter (2005), *Baroclinic Tides: Theoretical Modeling and Observational Evidence*, 351 pp., Cambridge University Press, Cambridge.

Weber, J. E. (1983), Steady Wind- and Wave-Induced Currents in the Open Ocean, *J. Phys. Oceanogr.*, *13*(3), 524-530.

Xing, J., and A. Davies (2009), Influence of bottom frictional effects in sill regions upon lee wave generation and implications for internal mixing, *Ocean Dynamics*, *59*(6), 837-861.

Ünlüata, Ü., and C. C. Mei (1970), Mass Transport in Water Waves, *J. Geophys. Res.*, *75*(36), 7611-7618.

I

JOURNAL OF GEOPHYSICAL RESEARCH, VOL. 115, C03022, doi:10.1029/2009JC005298, 2010

Mass transport induced by internal Kelvin waves beneath shore-fast ice

Eivind Støylen[1] and Jan Erik H. Weber[1]

Received 22 January 2009; revised 12 August 2009; accepted 28 October 2009; published 26 March 2010.

[1] A one-layer reduced-gravity model is used to investigate the wave-induced mass flux in internal Kelvin waves along a straight coast beneath shore-fast ice. The waves are generated by barotropic tidal pumping at narrow sounds, and the ice lid introduces a no-slip condition for the horizontal wave motion. The mean Lagrangian fluxes to second order in wave steepness are obtained by integrating the equations of momentum and mass between the material interface and the surface. The mean flow is forced by the conventional radiation stress for internal wave motion, the mean pressure gradient due to the sloping surface, and the frictional drag at the boundaries. The equations that govern the mean fluxes are expressed in terms of mean Eulerian variables, while the wave forcing terms are given by the horizontal divergence of the Stokes flux. Analytical results show that the effect of friction induces a mean Eulerian flux along the coast that is comparable to the Stokes flux. In addition, the horizontal divergence of the total mean flux along the coast induces a small mass flux in the cross-shore direction. This flux changes the mean thickness of the upper layer outside the trapping region and may facilitate geostrophically balanced boundary currents in enclosed basins. This is indeed demonstrated by numerical solutions of the flux equations for confined areas larger than the trapping region. Application of the theory to Arctic waters is discussed, with emphasis on the transport of biological material and pollutants in nearshore regions.

Citation: Støylen, E., and J. E. H. Weber (2010), Mass transport induced by internal Kelvin waves beneath shore-fast ice, *J. Geophys. Res.*, *115*, C03022, doi:10.1029/2009JC005298.

1. Introduction

[2] Waves propagating in a fluid induce a mean drift in the direction of the wave propagation. This classic result was first derived by *Stokes* [1847], who studied motion in inviscid fluids. *Longuet-Higgins* [1953] extended the analysis of wave-induced mean motion to viscous fluids. He showed that the mean Lagrangian drift velocity u_L is a sum of the Stokes drift velocity u_S and a mean Eulerian contribution u_E. The latter did depend on the effect of viscosity but not on the size of the viscosity coefficient.

[3] Studies of wave drift in various classes of surface waves in the open rotating ocean are numerous [e.g., *Madsen*, 1978; *Weber*, 1983; *Jenkins*, 1986; *Xu and Bowen*, 1994; *Bondarenko et al.*, 2004]. The presence of coasts may give rise to coastally trapped waves like edge waves and Kelvin waves. We will be concerned with the latter type here. Since the baroclinic (internal) Rossby radius of deformation usually is very much smaller than the barotropic one and the amplitudes of internal Kelvin waves often are much larger than the amplitudes of the surface modes, it is in fact the mean drift in internal coastal Kelvin waves that may affect nearshore conditions most severely. *Csanady* [1972] was apparently the first to suggest that the transport associated with internal Kelvin waves may have a significant impact on the transport of nearshore effluents in lakes. Motivated by this, *Wunsch* [1973] derived the solution for an internal Kelvin wave forced by wind stress. He then calculated the Stokes drift of this wave, assuming that the Eulerian drift contribution was negligible. His results indicated that drift in internal Kelvin waves may explain certain observed circulation patterns in lakes. *Ou and Bennett* [1979] argued that the Stokes drift itself was not observable by conventional current meters and that the Eulerian mean should be included in the derivations to the second order in wave amplitude. They studied a hypothetical circular lake, where the applied forcing was a horizontally uniform, diurnally oscillating wind stress. *Ou and Bennett* [1979] stated that the resulting drift pattern may explain observed circulation patterns in Lake Kinneret, Israel.

[4] As pointed out by *Wunsch* [1973], a variable wind stress can excite internal Kelvin waves. However, in layered systems with strong barotropic tidal flow over bottom sills, we may find pronounced internal waves [e.g., *Farmer and Smith*, 1980]. In Arctic regions, with ice cover for a long period of the year, the barotropic tide will constitute the main generating mechanism for internal waves. Along the Siberian Shelf and in the Canadian Archipelago we find considerable internal wave activity due to tidal forcing

[1]Department of Geosciences, University of Oslo, Oslo, Norway.

0148-0227/10/2009JC005298

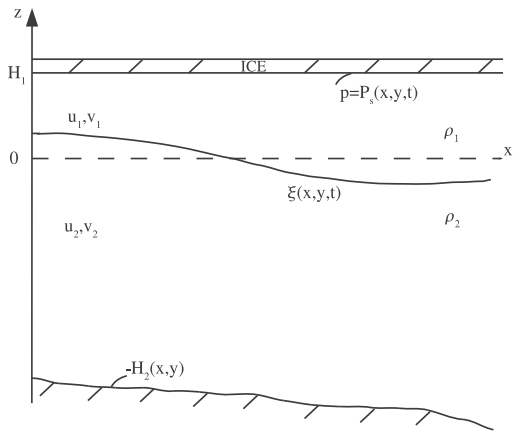

Figure 1. Sketch of the two-layer model with constant densities ρ_1 and ρ_2, horizontal coordinates (x, y), and horizontal current components ($u_{1,2}$, $v_{1,2}$). The straight coast is at $y = 0$, and the surface (rigid ice lid) and moving interface are given by $z = H_1$ and $z = \xi$, respectively. The one-layer reduced-gravity model requires $H_2 \gg H_1$.

[*Levine*, 1990; *Morozov and Pisarev*, 2002; *Morozov et al.*, 2003; *Morozov and Pisarev*, 2003; *Morozov et al.*, 2008]. The intention of this paper is to investigate theoretically the mean mass transport induced by internal Kelvin waves under such circumstances.

[5] The structure of this paper is as follows: In sections 2–4 we go through the mathematical background for this problem and derive analytical solutions for waves along a straight coast and the associated mean Lagrangian volume fluxes. In section 5 we solve the equations for the mean drift numerically in idealized regions that encompass the trapping region of internal Kelvin waves. In section 6 we run numerical models for realistic topography and compare the results with the former idealized cases. Section 7 discusses the application of the present theory to various regions in Arctic waters, and section 8 contains some concluding remarks.

2. Mathematical Formulation

[6] We consider internal Kelvin waves in a stably stratified two-layer system under an ice sheet that does not move in the horizontal directions (see Figure 1). The layers are incompressible and have densities ρ_1 and ρ_2. The motion is described in a Cartesian coordinate system (x, y, z), where the z axis is directed upward. The horizontally averaged position of the ice sheet is at $z = H_1$, and the interface between the layers is situated at $z = \xi$ (x, y, t), where t is time. We have a straight coast at $y = 0$ in our model. The waves propagate in the x direction, and the velocity is $\mathbf{u} = (u, v, w)$.

[7] The presence of an ice cover will generally affect the propagation of gravity waves (see, e.g., *Liu and Mollo-Christensen* [1988] in the case of surface waves). For internal waves in a continuously stratified ocean under ice, *Muzylev* [2008] showed that, because of the elastic properties of the ice, nonzero surface deflections occur for the lowest internal mode if the wave frequency ω is close to the buoyancy frequency N. However, when $\omega/N \ll 1$, corresponding to long waves, the rigid-lid approximation (negligible vertical deflection under the ice) is very well fulfilled. In the present problem we consider tidally generated waves. For the semidiurnal tide M_2 we have $\omega = 1.4 \times 10^{-4}$ s^{-1}, which is much smaller than the buoyancy frequency for a continuous stratification normally found in Arctic waters, where N may range from 10^{-3} to 5×10^{-2} s^{-1}, according to *Muzylev* [2008]. Hence, the rigid-lid approximation works well for the continuously stratified case. In the present two-layer case, we assume that the tidally forced waves are so long that we can make the hydrostatic approximation in both layers. Then the elastic plate terms in the pressure under the ice [*Liu and Mollo-Christensen*, 1988] become very much smaller than the acceleration due to gravity and can safely be neglected. Accordingly, the rigid-lid approximation can be applied to obtain the baroclinic response in our case. We also take the lower layer to be much deeper than the upper layer. Then we can apply a one-layer reduced-gravity model [*McCreary*, 1976; *Busalacchi and O'Brien*, 1980] for this problem. However, we retain the nonlinear terms in the upper layer to capture the mean wave-induced mass flux.

[8] In our problem the main effect of the stationary ice cover is that it acts as a sink of momentum through the effect of friction. For the wave motion we assume a viscous no-slip condition, while for the nonlinear mean volume fluxes we apply a turbulent frictional drag formulation.

3. Linear Waves

[9] In a one-layer reduced-gravity model, the velocities induced by internal waves are neglected in the deep lower layer. Hence, the balances of forces in the lower layer become

$$\begin{aligned} g\tilde{\eta}_x + P_{Sx}/\rho_1 &= -g'\tilde{\xi}_x, \\ g\tilde{\eta}_y + P_{Sy}/\rho_1 &= -g'\tilde{\xi}_y, \end{aligned} \tag{1}$$

where subscripts denote partial differentiation. Furthermore, $g' = g(\rho_2 - \rho_1)/\rho_1$ is the reduced gravity, $\tilde{\eta}$ is the linear surface deflection under the ice (not depicted in Figure 1), P_S is the variable pressure under the ice, and $\tilde{\xi}$ is the linear deflection of the interface between the layers. Because of the presence of a straight coast at $y = 0$, the first-order upper layer current component v_1 is zero everywhere. Utilizing the hydrostatic approximation in the upper layer and inserting for $g\tilde{\eta} + P_S/\rho_1$ from (1), we can write for the linearized momentum balance in the upper layer

$$\begin{aligned} u_{1t} &= g'\tilde{\xi}_x + \nu\nabla_h^2 u_1 + \nu u_{1zz}, \\ fu_1 &= g'\tilde{\xi}_y, \end{aligned} \tag{2}$$

where ν is the kinematic viscosity coefficient and f is the Coriolis parameter. The horizontal Laplacian operator ($\partial^2/\partial x^2 + \partial^2/\partial y^2$) is denoted by ∇_h^2. For the baroclinic response, we assume that $|\tilde{\xi}| \gg |\tilde{\eta}|$, which in effect is the rigid-lid

approximation. Then the linearized continuity equation in the upper layer reduces to

$$\tilde{\xi}_t = \frac{\partial}{\partial x}\int_0^{H_1} u_1\, dz. \tag{3}$$

[10] In this analysis we take the wave frequency ω to be constant, that is, for a complex Fourier component $u_{1t} = -i\omega u_1$. In order to resolve the dynamics under the ice, we separate the wave current into a depth-independent part, $\tilde{u}_1$, and a boundary layer part, $\hat{u}_1$:

$$u_1 = \tilde{u}_1(x, y, t) + \hat{u}_1(x, y, z, t), \tag{4}$$

where $\hat{u}_1$ is important only in a thin boundary layer below the ice. From (2) and (4), assuming that the vertical variation of $\hat{u}_1$ is much larger than the horizontal variation and applying a no-slip condition at the ice-water interface, we find

$$\hat{u}_1 = -\tilde{u}_1 \exp[-(1-i)(H_1 - z)/\delta], \tag{5}$$

where $\delta = \sqrt{2\nu/\omega}$ is the viscous boundary layer thickness. This is the classic Stokes oscillatory boundary layer solution near a smooth wall (see the review by *Mei* [1989]). We assume here that $\delta \ll H_1$. We have also neglected the frictional influence from the vertical coast. This is justified by the fact that the depth of the upper layer is much smaller than the internal Rossby radius, which sets the horizontal scale under the ice. From (3) we then obtain

$$\tilde{\xi}_t = H_1\tilde{u}_{1x} + \frac{\partial}{\partial x}\int_0^{H_1} \hat{u}_1 dz. \tag{6}$$

By combining (2) and (6), we readily find for the barotropic part of the wave velocity in the upper layer

$$(1 - i\varepsilon)\tilde{u}_{1xx} + \frac{\omega^2}{g'H_1}\tilde{u} = 0, \tag{7}$$

$$(1 - i\varepsilon)\tilde{u} = \frac{g'}{f}\tilde{\xi}_y, \tag{8}$$

$$-\frac{g'H_1}{\omega^2}\tilde{u}_{1xxt} + (1-i)\varepsilon\frac{g'H_1}{\omega}\tilde{u}_{1xx} = g'\tilde{\xi}. \tag{9}$$

These equations are valid to first order in wave steepness and contain the lowest-order correction in the small parameter $\varepsilon = \delta/2H_1$.

[11] We assume for the internal wave that

$$\tilde{\xi} = Ae^{-\alpha x - y/a}e^{i\psi}, \tag{10}$$

where A is the amplitude and $\psi = kx + ly - \omega t$ is the phase function with wave numbers k and l. The wave propagates along the positive x axis with $k > 0$. Furthermore, α is a spatial damping coefficient, and a is the internal Rossby radius. Inserting (10) into (7)–(9) and letting the real part represent the physical solution, we obtain for the wave motion

$$\tilde{\xi} = Ae^{-\alpha x - y/a}\cos\ \psi, \tag{11}$$

$$\tilde{u}_1 = -\frac{c_1 A}{H_1}e^{-\alpha x - y/a}\left(\cos\ \psi - \frac{\varepsilon}{2}\sin\ \psi\right), \tag{12}$$

$$\hat{u}_1 = \frac{c_1 A}{H_1}e^{-\alpha x - y/a}e^{-q} \cdot \left[\left(\cos q - \frac{\varepsilon}{2}\sin q\right)\cos\ \psi - \left(\sin q + \frac{\varepsilon}{2}\cos q\right)\sin\ \psi\right], \tag{13}$$

where $c_1 = \omega/k$ is the phase speed of the internal wave and $a = c_1/f$. Furthermore, we have defined $q = (H_1 - z)/\delta$. From the dispersion relation we find that $\omega^2 = g'H_1k^2$ to lowest order, while the small wave number in the direction normal to the coast is $l = \varepsilon f/2c_1$. The spatial attenuation coefficient is given by $\alpha = \varepsilon k/2$. As shown by *Melsom* [1992], the wave damping coefficient is influenced by the elastic properties of the ice cover. However, for long waves this effect becomes negligible. Equations (11) and (12) describe spatially damped internal Kelvin waves with cophase lines that are tilted backward from the coast [e.g., *Martinsen and Weber*, 1981]. This effect was noted by *Fjeldstad* [1929] and *Mofjeld* [1980] for barotropic Kelvin waves and by *Brink and Allen* [1978] for barotropic vorticity waves over a sloping continental shelf.

4. Nonlinear Analysis for a Straight Wall

[12] The nonlinear mean Lagrangian upper layer volume fluxes $\overline{U}$ and $\overline{V}$ are obtained by integrating the governing Eulerian equations in the vertical wall between the material interface ξ and the surface H_1 (see *Phillips* [1977] or *Weber et al.* [2006] in the case of surface waves). Here the overbar denotes average over the wave period $2\pi/\omega$. We separate the fluctuating and the mean parts of the motion by writing all the variables in the form

$$U = \tilde{U} + \overline{U}. \tag{14}$$

From the integrated momentum and continuity equations we then find for the steady mean Lagrangian fluxes in the upper layer, correct to second order in wave steepness,

$$-f\overline{V} - c_1^2\overline{\xi}_x = R_1 + \tau_s^{(x)}/\rho_1 - \tau_i^{(x)}/\rho_1, \tag{15}$$

$$f\overline{U} - c_1^2\overline{\xi}_y = R_2 + \tau_s^{(y)}/\rho_1 - \tau_i^{(y)}/\rho_1, \tag{16}$$

$$\overline{U}_x + \overline{V}_y = 0. \tag{17}$$

Here $(\tau_s^{(x)}, \tau_s^{(y)})$ and $(\tau_i^{(x)}, \tau_i^{(y)})$ are the surface and the interfacial stress components, respectively. The nonlinear wave forcing terms R_1 and R_2 become

$$R_1 = -\frac{g'}{2}\frac{\partial}{\partial x}\overline{\xi^2} - \frac{\partial}{\partial x}\overline{\int_0^{H_1} u_1^2\, dz} \tag{18}$$

$$R_2 = -\frac{g'}{2}\frac{\partial}{\partial y}\overline{\xi^2}. \tag{19}$$

According to *Longuet-Higgins* [1953], the mean Lagrangian flux terms can be split into a Stokes flux and an Eulerian flux, that is, $\overline{U}_L = \overline{U}_S + \overline{U}_E$ and $\overline{V}_L = \overline{V}_S + \overline{V}_E$. The Stokes fluxes for this problem become

$$\overline{U}_S = \int_0^{H_1} \overline{\left(\int u_1 dt\right) u_{1x}} dz = \frac{c_1 A^2}{2H_1} e^{-2(\alpha x + y/a)}, \qquad \overline{V}_S = 0. \tag{20}$$

By inserting equations (11)–(13) into (18) and (19), we realize that the wave forcing terms may be expressed in terms of the Stokes fluxes (20):

$$R_1 = -(3/2) c_1 \overline{U}_{Sx}, \tag{21}$$

$$R_2 = f \overline{U}_S. \tag{22}$$

We note that (21) is just the internal shallow-water wave parallel to the radiation stress term of *Longuet-Higgins and Stewart* [1962].

[13] The effect of friction is important in wave problems. Without friction, we would be left with an undamped Stokes flux in this case. The effect of friction is to induce an additional mean Eulerian flow. In the laminar model of *Longuet-Higgins* [1953] the effect of molecular viscosity induces secondary mean Eulerian momentum at the bottom of the tank (through a no-slip condition). When this momentum has diffused through the fluid, the resulting mean Eulerian volume flux for shallow-water waves is 3/2 times the Stokes flux. Of course, the situation is different for a turbulent ocean, but not qualitatively. The effect of friction must still induce an additional mean Eulerian flow.

[14] In (15) and (16) the under-ice stress (surface stress) is assumed to be much larger than the interfacial stresses; that is, $|\tau_s| \gg |\tau_i|$. It is not trivial to model $\boldsymbol{\tau}_s$, but here we use the similarity with the familiar storm surge problem and take the stress components at a rigid plane to be proportional to the square of the mean Eulerian velocities. Hence,

$$\tau_s/\rho_1 = -c_D \left(\overline{U}_E^2 + \overline{V}_E^2\right)^{1/2} \overline{\mathbf{U}}_E / H_1^2, \tag{23}$$

where c_D is a dimensionless drag coefficient. We may expect the mean cross-wall Eulerian velocity $\overline{V}_E/H_1$ to be small in this problem, so the effect of friction can be neglected in (16). Since $\overline{U} = \overline{U}_L$ and $\overline{V} = \overline{V}_L$ in the present analysis, we can use (20)–(23) to express (15)–(17) entirely in terms of the mean Eulerian fluxes:

$$-f \overline{V}_E - c_1^2 \overline{\xi}_x = -(3/2) c_1 \overline{U}_{Sx} - c_D \left|\overline{U}_E\right| \overline{U}_E / H_1^2, \tag{24}$$

$$f \overline{U}_E - c_1^2 \overline{\xi}_y = 0, \tag{25}$$

$$\overline{U}_{Ex} + \overline{V}_{Ey} = -\overline{U}_{Sx}. \tag{26}$$

These equations resemble the steady barotropic storm surge problem, but the forcing here in the momentum equation is not from the wind stress but from the horizontal divergence of the Stokes flux (or the radiation stress). Note the extra forcing term in the continuity equation, which is not present in surge models. This specific feature related to wave drift was first pointed out by *Dolata and Rosenthal* [1984]. We note from (25) that, in the absence of friction in the y direction, the mean Eulerian flow is geostrophically balanced in the direction normal to the coast. It is easy to obtain from (24)–(26)

$$-4\alpha f \overline{U}_S = \frac{c_D}{H_1^2} \left(\left|\overline{U}_E\right| \overline{U}_E\right)_y, \tag{27}$$

which shows that $\overline{U}_E > 0$ for coastally trapped motion. We realize from (27) that the frictional wave attenuation coefficient must approach zero in the same way as the drag coefficient for the mean flow, that is, $O(\alpha H_1) \sim O(c_D)$. If we require that $\overline{\xi}$ approaches zero for large x, the solutions to equations (24)–(26) are

$$\overline{U}_E = \sqrt{\frac{\alpha H_1}{c_D}} c_1 A e^{-\alpha x - y/a}, \tag{28}$$

$$\overline{V}_E = \alpha a c_1 A \left[\frac{A}{2H_1}\left(1 - e^{-2y/a}\right) e^{-2\alpha x} + \sqrt{\frac{\alpha H_1}{c_D}}\left(1 - e^{-y/a}\right) e^{-\alpha x}\right], \tag{29}$$

$$\overline{\xi} = \frac{A}{4H_1} A e^{-2\alpha x} + \sqrt{\frac{\alpha H_1}{c_D}} A \left(1 - e^{-y/a}\right)\ e^{-\alpha x}. \tag{30}$$

[15] To assess the magnitude of the along-shore Eulerian flux $\overline{U}_E$, we use typical parameters from the eastern Barents Sea [*Loeng*, 1991]. A typical internal wave amplitude in this region is 8 m [*Morozov and Pisarev*, 2003]. Concerning the drag coefficient, *Nøst* [1994] uses $c_D = 1 \times 10^{-3}$ for the drag coefficient under ice, while *Dmitriev et al.* [1991] apply the value $c_D = 5.5 \times 10^{-3}$. *Melsom* [1992] reports that an eddy viscosity of 1.5×10^{-4} m^2 s^{-1} fits observational data for spatial damping of surface waves in the presence of an ice cover quite well. In the calculations of the mean drift he takes $\nu = 1 \times 10^{-3}$ m^2 s^{-1}. *Weber* [1987] estimates values of ν from two separate field data sets to be 4×10^{-4} and 2×10^{-3} m^2 s^{-1}. Here the latter value is probably on the higher side since it also models energy loss due to ice floe collisions. Middle-of-the-road values for the physical parameters are listed in Table 1. Inserting for these parameters in (28), we find that $\overline{U}_E = 2.2\ \overline{U}_S$ at the coast, which compares well with Longuet-Higgins' result, $\overline{U}_E = (3/2)\ \overline{U}_S$, for laminar flow.

[16] We note from (29) that the mean Eulerian flux has a small nonvanishing component in the direction normal to the coast. This is due to the horizontal divergence of the along-shore flux, as can be inferred from the presence of the small damping factor $\alpha = [\nu k^2/(8\omega H_1^2)]^{1/2}$. In the trapping region the mean velocity $\overline{V}_E/H_1$ is much smaller than the along-shore mean velocities (for the parameters in this example $\overline{V}_E = 0.02\overline{U}_E$), which justifies our previous neglect of this velocity component in modeling the frictional stress (equation (23)).

[17] We note from (29) that $\overline{V}_E$ is zero at the coast and attains its maximum value just outside the trapping region. The cross-shore mass transport induced by the frictional damping of the mean along-shore Lagrangian flux has not

Table 1. Physical Parameters

H_1 (m)	ω (s^{-1})	g' (ms^{-2})	c_1 (m s^{-1})	ν (m^2 s^{-1})	c_D	a (km)	λ (km)	$1/\alpha$ (km)
			Eastern Barents Sea and Closed-Box Model					
40	1.4×10^{-4}	0.01	0.63	5×10^{-4}	3×10^{-3}	4.5	28	270
			Rectangular Fjord Model and the Van Mijen Fjord					
30	1.4×10^{-4}	0.01	0.55	irrelevant	irrelevant	3.9	25	176
			Baffin Bay					
100	1.4×10^{-4}	0.01	1.0	5×10^{-4}	3×10^{-3}	7.1	45	1069

been reported in the literature before. This flux has important consequences since it leads to a seaward mass accumulation and an associated change of upper layer thickness. This, in turn, may induce a geostrophic return flow in the area outside the trapping region. We will come back to this problem in section 5, where we present results from a numerical computation in a confined area that is larger than the trapping region.

5. Mean Flow Due to Internal Kelvin Waves in an Enclosed Basin

[18] As demonstrated in section 4, internal Kelvin waves along a straight coast will affect the conditions outside the trapping region of the wave. The motion here cannot be resolved analytically, so we have to solve our system of equations (24)–(26) numerically. We apply a simple rectangular geometry. The model domain is a 160 km × 80 km closed box with a grid size of 200 m. The internal wave is present at the lower boundary, and the setting simulates wave generation in a narrow sound in the lower left corner. The nonlinear forcing term in this case is just the damped Stokes flux (equation (20)), which we have determined analytically. Some details of the numerical two-layer model are given in Appendix A. In the current model setup, we utilize a reduced-gravity mode, where only upper layer fluxes and interface elevations are calculated. The surface elevation is neglected because of the presence of rigid ice. The lower layer is assumed to be infinitely deep, so that the lower layer current can be ignored. For numerical reasons we reintroduce the Lagrangian fluxes and the small friction term $\tau_S^{(y)}$ in the y direction in (24)–(26).

[19] We choose the same model parameters as in section 4 (see Table 1), with an internal wave amplitude of 8 m. This yields an analytical mean current $(\overline{U}_E + \overline{U}_S)/H_1 = 4$ cm s^{-1} at the lower left corner. The numerical results are presented in Figures 2 and 3 for the upper layer current and the mean interface elevation, respectively. The intensified current along the lower wall is evident, with maximum amplitudes of around 3 cm s^{-1}. From Figure 3 we note that the interface maximum is located just outside the forcing region, in accordance with the analytical solution (equation (30)). There is almost no interface displacement in the interior, and near the sidewalls and the upper wall the interface becomes increasingly negative. The resulting pressure gradient drives a boundary flow in quasi-geostrophic balance, as shown in Figure 2. We also note from Figure 2 that we have an intensified return current just outside the trapping region. This is caused by the pressure gradient associated with the transition between the forced lower boundary and the interior at rest.

[20] In the rectangular model run, the solutions near the lower corners are not necessarily physical. To validate the solution here, we perform another model run in a geometry without corners. We consider a circular basin with radius 100 km (see Figure 4a). A wave stress is applied, with maximum amplitude at the bottom, to the right of the line at $x = 100$ km, as indicated in Figure 4a. The stress is decreasing counterclockwise along the coast. The wave generation area, shown between the two radial lines in Figure 4a, is parameterized as a strongly increased friction coefficient along with a linear change of wave stress to avoid discontinuity in the forcing. Results for interface displacement and current magnitude and direction are shown in Figures 4a and 4b, respectively. The resemblance to the solution for a rectangular geometry is evident. The magnitudes are comparable, and the

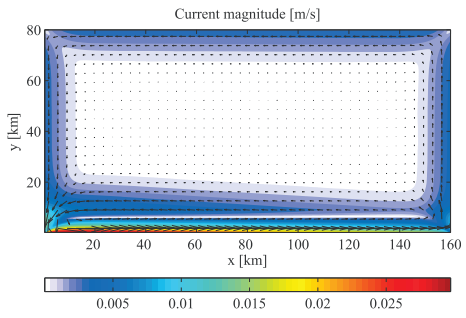

Figure 2. Mean current magnitude and direction for the rectangular numerical model run in section 5.

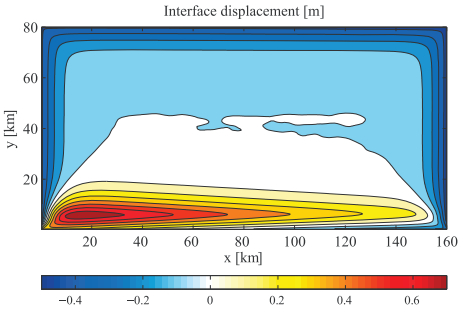

Figure 3. Interface displacement from the rectangular numerical model run discussed in section 5. Near the lower wall the interface displacement is positive, whereas it is negative in the upper region.

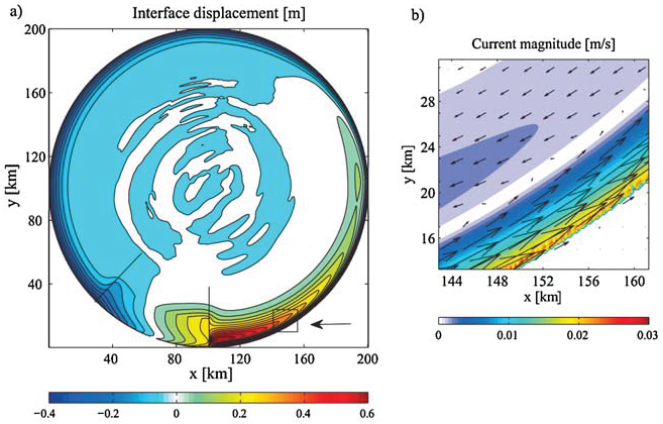

Figure 4. (a) Interface displacement and (b) mean current magnitude and direction from the circular numerical model run discussed in section 5. The box in Figure 4a shows the boundaries of the enlarged area in Figure 4b. The radial black lines in Figure 4a show the boundaries of the region with enhanced friction simulating wave generation. Positive displacement values are evident in the lower right part of the domain, and displacements are negative in the upper left part.

currents follow the isobars. From Figure 4b we observe a small current component normal to the coast due to the along-coastal decay in wave amplitude.

[21] The maximum current values are somewhat smaller than what we would expect from the analytical result, although they are within a reasonable order of magnitude. Because of the experimental nature of this model setup, the quantitative nature of the solution should be viewed with some caution. In particular, the corners in the rectangular model run and the wave generation area in the circular run provide unphysical contributions to the solution. Still, the similarity of the two solutions strongly suggests that these effects are of minor importance to the general solution away from the wave generation area.

6. Internal Kelvin Waves With Realistic Topography

[22] The theory presented in sections 2–4 is strictly valid for a straight vertical wall and an infinitely deep lower layer. These conditions are hardly met in nature, so it is of interest to investigate whether we may expect similar results when the topography gets more complex. In the following we present a new set of numerical results where a full two-layer model is applied. The simulations are made for two different bottom and coastal topographies. The first is a rectangular fjord model; the second is the Van Mijen fjord in Svalbard, Norway (see Figure 5).

[23] Results from the run with a rectangular fjord are shown in Figure 6 [see also *Støylen*, 2008]. At the lower left corner of the fjord there is a narrow sound of depth 35 m. The forcing in the outer part is a surface oscillation with the M_2 tidal period of 12.4 h. The grid size is 200 m, and the physical parameters are given in Table 1. The plot shows amplitudes of interface displacement, normalized with respect to the maximum amplitude. Numerical values of the amplitudes are not shown, as the model does not resolve energy loss due to turbulence at the sound properly. Surface amplitudes (not shown) are about 1/10 of the interface

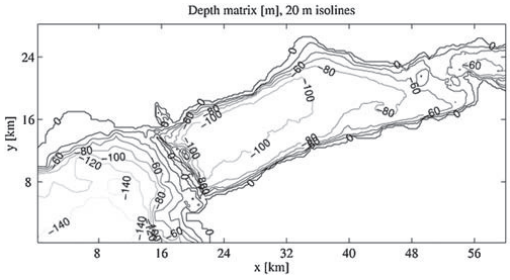

Figure 5. Coastline and bottom topography in the Van Mijen fjord in Svalbard, situated at 77.8°N, 15.5°E. Akseløya is displayed in gray.

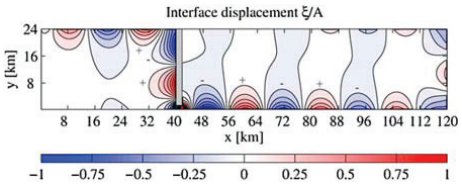

Figure 6. Interface displacement in a rectangular fjord from a linear two-layer model simulation. Amplitudes are normalized with respect to maximum amplitude A. To the left of the barrier (island), the surface oscillates with the tidal M_2 frequency. The boundary at $x = 0$ is open. Plus and minus signs depict positive and negative displacements, respectively.

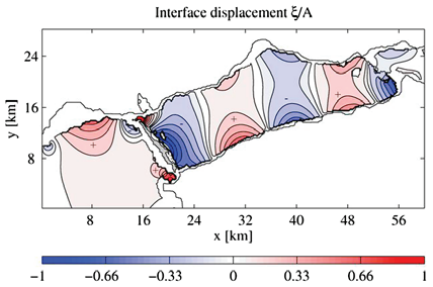

Figure 7. Interface displacement in the Van Mijen fjord (77.8°N, 15.5°E) from a linear numerical model run. Plus and minus signs depict positive and negative displacements, respectively, and amplitudes are normalized, as in Figure 6. The contours are plotted along the 30 m isobaths.

amplitudes. We see from Figure 6 that internal wave generation occurs at the sound as predicted by theory. The amplitudes are largest near the sound and decay horizontally due to friction. The trapped motion near the coast shows a propagating Kelvin wave. From Figure 6, a rough estimate of the wavelength and the Rossby radius of deformation yields 22 and 4 km, respectively, which are fairly well in accordance with the theoretical values in Table 1.

[24] From Figure 5 we note that the island Akseløya is nearly blocking the entrance to the Van Mijen fjord in Svalbard. This island prevents ice from being transported out of the fjord by the action of the wind. Consequently, fast ice remains in the fjord a large part of the year [*Fer and Widell*, 2007]. North and south of Akseløya are two sounds, Akselsundet and Mariasundet, respectively, where internal wave generation may take place. It should be emphasized that we are not attempting to describe the actual internal wave patterns in this particular fjord. We are merely using the realistic topography, together with an idealized two-layer density distribution, to study the resulting motion (a pronounced two-layer structure is in fact most typical for a summer–early autumn situation in the Van Mijen fjord). The physical parameters are the same as in the previous rectangular fjord run (see Table 1). The numerical result is presented in Figure 7. When we take into account the complex topography of the Van Mijen fjord, with a possible wave generation at both sounds, the similarity of the propagating internal wave pattern at the lower boundary between the two cases depicted in Figures 6 and 7 is indeed amazing. We conclude that the generation and propagation of internal Kelvin waves caused by the barotropic tide over rapidly changing bottom topography is a robust phenomenon. A sloping bottom near the coast does not obstruct the wave propagation. However, it may support additional edge waves, which are not studied here. Nor do deviations from a straight coast seem to play any important role.

7. Discussion

[25] In sections 2–4 we developed a theory for the mean Lagrangian fluxes induced by internal Kelvin waves propagating along a vertical wall. We demonstrated numerically that these waves do retain their properties for more complex geometries. Accordingly, after the waves have been generated, they should be able to propagate freely along the boundary. The wave amplitude is decaying because of friction, which is predominantly due to drag from the ice in winter Arctic regions. Generation areas should be regions where strong barotropic tides interact with rapid changes in topography. We would like to assess mean wave-induced velocities in the upper layer and relate them to the physical ocean. Since our theoretical along-shore flux actually has a maximum at the coast, where in practice the conditions are far from ideal, we chose to define more robust mean velocity components in the trapping region. Since the fluxes varies much more rapidly in the cross-coast direction than along the coast, we may define typical mean Stokes and mean Eulerian drift components as

$$\langle u_S \rangle = \frac{1}{aH_1}\int_0^a \overline{U}_S\, dy, \quad \langle u_E \rangle = \frac{1}{aH_1}\int_0^a \overline{U}_E\, dy, \quad \langle v_E \rangle = \frac{1}{aH_1}\int_0^a \overline{V}_E\, dy. \tag{31}$$

[26] We focus first on the eastern Barents Sea, where there is an ice cover in winter. The entire region is stratified and tidally energetic [*Gjevik et al.*, 1994; *Padman and Erofeeva*, 2004]. In addition, we are close to the critical latitude for the M_2 tidal component. Classical theory states that free waves of such frequency are suppressed in this region [*LeBlond and Mysak*, 1978], although forced nonlinear internal waves of short wavelengths are still present [*Vlasenko et al.*, 2003]. The linear internal tides are restricted to follow topographic features [*Wunsch*, 1975], with a quasi-geostrophic balance in the direction normal to the boundary. We thus expect the Barents Sea to be an area where the internal Kelvin wave may be a significant contributor to the internal wavefield. Numerical simulations by *Morozov and Pisarev* [2003] show that the internal tide in this region is indeed confined to coastal areas (see Figure 8). We note amplitudes near the coast of order 10 m, indicating that internal wave transport is significant in this region.

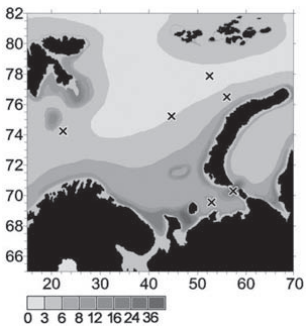

Figure 8. Map of internal tide amplitudes (in meters) from a numerical model in the Barents Sea. Crosses indicate stations where results are compared with measurements. Axes depict degrees east and north. From *Morozov and Pisarev* [2003].

[27] In Arctic waters the density stratification varies with time. In the autumn, just before the ice season, the two-layer stratification is most pronounced. When freezing commences, haline convection leads to vertical mixing, which weakens the stratification. When the ice extent is at its largest in the spring (March), the upper 200 m are almost homogeneous in density. Typically, $(\rho_2 - \rho_1)/\rho_1 \approx 10^{-3}$ for the early freezing period in this region [*Loeng*, 1991]. The relevant parameters are displayed in Table 1. From *Morozov and Pisarev* [2003] we take A to be 8 m. Then, from (31) evaluated at $x = 0$, we obtain for the mean along-shore velocity components $\langle u_S \rangle = 0.5$ cm s^{-1} and $\langle u_E \rangle = 1.8$ cm s^{-1}. Note that the Eulerian and Stokes drift contributions are of comparable magnitude but that the Eulerian drift velocity is definitely the largest. The mean velocity $\langle v_E \rangle$ normal to the coast in this case is 0.03 cm s^{-1}, which is hardly measurable.

[28] Similar conditions are met in other parts of the Arctic, for example, in Baffin Bay. This region is partly ice covered most of the year, with only near-ice-free conditions in August and September. In March the entire sea, except the eastern Davis Strait, is ice covered [*Tang et al.*, 2004]. Numerical simulations indicate that the Davis Strait is a tidally energetic area. *Padman and Erofeeva* [2004] report mean tidal current speeds of 10–20 cm s^{-1} on the eastern continental shelf. Across the continental shelf in eastern Baffin Bay there are several deep canyons where the strong barotropic tide may induce internal wave motion in the pycnocline. For the density distribution, we refer again to *Tang et al.* [2004]. From their November data we estimate roughly an upper layer thickness H_1 of 100 m. The mean upper layer temperature and salinity are 1°C and 33 psu, respectively. The corresponding lower layer values are 2.5°C and 34 psu, respectively. Thus, the upper and lower layer densities ρ_1 and ρ_2 are 1027 and 1028 kg m^{-3}, respectively. The relevant parameters for our calculations are listed in Table 1. The wavelength λ in this example is of order 50 km, yielding $a \ll \lambda \ll 1/\alpha$, as presupposed by our theory. To quantify the wave drift, we need information on the internal wave amplitude. Without direct measurements or numerical estimates of the baroclinic velocities, we can only make crude assumptions. Accordingly, assume that the internal wave amplitude is one fifth of the upper layer thickness, which is not uncommon in such systems, that is, $A = 20$ m. For the maximum mean drift along the coast in Baffin Bay we then obtain $\langle u_S \rangle = 0.9$ cm s^{-1} and $\langle u_E \rangle = 2.2$ cm s^{-1}. As in the Barents Sea, the Eulerian and Stokes drift contributions are of comparable magnitude, with the Eulerian part being the larger. The maximum mean normal velocity is again very small ($\langle v_E \rangle = 0.02$ cm s^{-1}).

8. Concluding Remarks

[29] We have seen that mean currents associated with tidally generated internal Kelvin waves under ice reach significant values near the shore in Arctic waters. Since these currents are always directed with the coast to the right (in the Northern Hemisphere), they yield a systematic transport in one particular direction. This may lead to accumulation or deposition of pollutants, oil spill, and biological material in certain areas along the coast. In enclosed basins, with internal wave generation at a sill, this systematic transport of mass along the boundaries may induce a permanent wave-induced circulation in the entire basin.

[30] The drift currents induced by internal Kelvin waves may affect the Barents Sea region in various ways. First, the eastern Barents Sea is exposed to radioactive pollution from nuclear activity and leakage from radioactive waste deposits. It is of considerable importance to identify the processes that influence the distribution of these pollutants [e.g., *Pavlov and Pfirman*, 1995]. Obviously, the systematic boundary-trapped drift discussed in this paper can be instrumental in advecting such material. Second, the Barents Sea region has been experiencing an increasing activity in offshore oil and gas exploration, which will inevitably lead to oil spill on various scales. Subsea oil leakage may accumulate under the ice and can be transported hundred of kilometers along the shore by the wave-induced drift derived here. Apart from the obvious environmental problem this causes, such transport of oil spill may also harm the population of ice algae living under the ice. These algae play an important role in the primary production of the Arctic ecosystem and are susceptible to oil pollution.

[31] The presence of ice enhances the mean Eulerian part of the wave drift through a stronger effect of friction. However, the drift induced by internal Kelvin waves is important even when the surface is ice free. Then the main frictional influence will occur at the top of the thermocline, which will yield a smaller wave damping and hence a smaller radiation stress. However, even without frictional effects at all, that is, vanishing Eulerian mean currents, the various examples from the Arctic in this paper show that the tidally generated internal Stokes drift yields a mean current that is comparable in magnitude to the climatologically permanent currents in this region. In addition, for ice-free conditions, the effect of the wind through a periodically varying wind stress can generate internal Kelvin waves, as discussed in section 1. It is also a fact that the two-layer structure in the Arctic is more pronounced in the summer, which in turn facilitates internal wave generation. Although we have focused on the drift due to internal Kelvin waves under ice, we may conclude that this drift is an important factor for the transport of upper layer material along the Arctic coasts the year-round.

Appendix A: Numerical Model

[32] The model is run either in a reduced-gravity mode, calculating vertically integrated upper layer fluxes and interface, or in a two-layer mode, where fluxes are calculated in both layers along with surface and interface elevations. Input parameters are relative density difference $\Delta\rho/\rho$, mean upper layer thickness H_1, Coriolis parameter f, gravity g, frictional drag coefficient c_D, and grid size Δs of the predetermined rectangular bottom topography matrix. The time step is determined from the Courant-Friedrichs-Lewy criteria. The computations are performed on a forward-backward C grid as explained by *Hjelmervik et al.* [2005]. Forcing may be applied as tidal oscillations or as inflow-outflow across an open boundary. In section 5 the program code is modified to include wave stress terms in the model equations.

[33] **Acknowledgments.** The authors would like to thank B. Gjevik for providing the numerical model and the bottom topography of the Van Mijen fjord. They are also indebted to E. Morozov for valuable discussions.

References

Bondarenko, A. L., V. V. Zhmur, Y. G. Filippov, and V. A. Shchev'ev (2004), On the transport of water masses by long-period waves in seas and oceans, *Phys. Oceanogr.*, *14*(5), 275–283, doi:10.1007/s11110-005-0008-3.

Brink, K. H., and J. S. Allen (1978), On the effect of bottom friction on barotropic motion over the continental shelf, *J. Phys. Oceanogr.*, *8*(5), 919–922, doi:10.1175/1520-0485(1978)008<0919:OTEOBF>2.0.CO;2.

Busalacchi, A. J., and J. J. O'Brien (1980), The seasonal variability in a model of the tropical pacific, *J. Phys. Oceanogr.*, *10*(12), 1929–1951, doi:10.1175/1520-0485(1980)010<1929:TSVIAM>2.0.CO;2.

Csanady, G. T. (1972), Response of large stratified lakes to wind, *J. Phys. Oceanogr.*, *2*(1), 3–13, doi:10.1175/1520-0485(1972)002<0003:ROLSLT>2.0.CO;2.

Dmitriev, N. E., A. Y. U. Proshutinsky, T. B. Løyning, and T. Vinje (1991), Tidal ice dynamics in the area of Svalbard and Frans Josef Land, *Polar Res.*, *9*(2), 193–205, doi:10.1111/j.1751-8369.1991.tb00614.x.

Dolata, L. F., and W. Rosenthal (1984), Wave setup and wave-induced currents in coastal zones, *J. Geophys. Res.*, *89*(C2), 1973–1982, doi:10.1029/JC089iC02p01973.

Farmer, D. M., and J. D. Smith (1980), Tidal interaction of stratified flow with a sill in Knight Inlet, *Deep Sea Res., Part A*, *27*, 239–254, doi:10.1016/0198-0149(80)90015-1.

Fer, I., and K. Widell (2007), Early spring turbulent mixing in an ice-covered Arctic fjord during transition to melting, *Cont. Shelf Res.*, *27*, 1980–1999, doi:10.1016/j.csr.2007.04.003.

Fjeldstad, J. E. (1929), *Contribution to the Dynamics of Free Progressive Tidal Waves*, Grieg, Bergen, Norway.

Gjevik, B., E. Nøst, and T. Straume (1994), Model simulations of the tides in the Barents Sea, *J. Geophys. Res.*, *99*(C2), 3337–3350, doi:10.1029/93JC02743.

Hjelmervik, K., A. Ommundsen, and B. Gjevik (2005), Implementation of non-linear advection terms in a high resolution tidal model, report, Dep. of Math., Univ. of Oslo, Oslo.

Jenkins, A. D. (1986), A theory for steady and variable wind- and wave-induced currents, *J. Phys. Oceanogr.*, *16*(8), 1370–1377, doi:10.1175/1520-0485(1986)016<1370:ATFSAV>2.0.CO;2.

LeBlond, P. H., and L. A. Mysak (1978), *Waves in the Ocean*, Elsevier, Amsterdam.

Levine, M. D. (1990), Internal waves under the Arctic pack ice during the Arctic Internal Wave Experiment: The coherence structure, *J. Geophys. Res.*, *95*(C5), 7347–7357, doi:10.1029/JC095iC05p07347.

Liu, A. K., and E. Mollo-Christensen (1988), Wave propagation in a solid ice pack, *J. Phys. Oceanogr.*, *18*(11), 1702–1712, doi:10.1175/1520-0485(1988)018<1702:WPIASI>2.0.CO;2.

Loeng, H. (1991), Features of the physical oceanographic conditions of the Barents Sea, *Polar Res.*, *10*(1), 5–18, doi:10.1111/j.1751-8369.1991.tb00630.x.

Longuet-Higgins, M. S. (1953), Mass transport in water waves, *Philos. Trans. R. Soc. London, Ser. A*, *245*(903), 535–581, doi:10.1098/rsta.1953.0006.

Longuet-Higgins, M. S., and R. W. Stewart (1962), Radiation stress and mass transport in gravity waves, with application to "surf-beats," *J. Fluid Mech.*, *13*(4), 481–504, doi:10.1017/S0022112062000877.

Madsen, O. S. (1978), Mass transport in deep-water waves, *J. Phys. Oceanogr.*, *8*(6), 1009–1015, doi:10.1175/1520-0485(1978)008<1009:MTIDWW>2.0.CO;2.

Martinsen, E. A., and J. E. Weber (1981), Frictional influence on internal Kelvin waves, *Tellus*, *33*, 402–410.

McCreary, J. (1976), Eastern tropical ocean response to changing wind systems: With application to El Niño, *J. Phys. Oceanogr.*, *6*(5), 632–645, doi:10.1175/1520-0485(1976)006<0632:ETORTC>2.0.CO;2.

Mei, C. C. (1989), *The Applied Dynamics of Ocean Surface Waves*, *Adv. Ser. Oceangr. Eng.*, World Sci., Singapore.

Melsom, A. (1992), Wave-induced roll motion beneath an ice cover, *J. Phys. Oceanogr.*, *22*(1), 19–28, doi:10.1175/1520-0485(1992)022<0019:WIRMBA>2.0.CO;2.

Mofjeld, H. O. (1980), Effects of vertical viscosity on Kelvin waves, *J. Phys. Oceanogr.*, *10*(7), 1039–1050, doi:10.1175/1520-0485(1980)010<1039:EOVVOK>2.0.CO;2.

Morozov, E. G., and S. V. Pisarev (2002), Internal tides at the Arctic latitudes (numerical experiments), *Oceanology, Engl. Transl.*, *42*(2), 153–161.

Morozov, E. G., and S. V. Pisarev (2003), Internal tidal waves in the Barents Sea, *Dokl. Earth Sci.*, *393*(8), 1124–1126.

Morozov, E. G., G. Parrilla-Barrera, M. G. Velarde, and A. D. Scherbinin (2003), The straits of Gibraltar and Kara Gates: A comparison of internal tides, *Oceanol. Acta*, *26*(3), 231–241, doi:10.1016/S0399-1784(03)00023-9.

Morozov, E. G., V. T. Paka, and V. V. Bakhanov (2008), Strong internal tides in the Kara Gates Strait, *Geophys. Res. Lett.*, *35*, L16603, doi:10.1029/2008GL033804.

Muzylev, S. V. (2008), Internal waves under ice cover, *Dokl. Earth Sci.*, *418*(1), 145–148, doi:10.1134/S1028334X08010327.

Nøst, E. (1994), Calculating tidal current profiles from vertically integrated models near the critical latitude in the Barents Sea, *J. Geophys. Res.*, *99*(C4), 7885–7901, doi:10.1029/93JC03485.

Ou, H. W., and J. R. Bennett (1979), A theory of the mean flow driven by long internal waves in a rotating basin, with application to Lake Kinneret, *J. Phys. Oceanogr.*, *9*(6), 1112–1125, doi:10.1175/1520-0485(1979)009<1112:ATOTMF>2.0.CO;2.

Padman, L., and S. Erofeeva (2004), A barotropic inverse tidal model for the Arctic Ocean, *Geophys. Res. Lett.*, *31*, L02303, doi:10.1029/2003GL019003.

Pavlov, V. K., and S. L. Pfirman (1995), Hydrographic structure and variability of the Kara Sea: Implications for pollutant distribution, *Deep Sea Res., Part II*, *42*, 1369–1390, doi:10.1016/0967-0645(95)00046-1.

Phillips, O. M. (1977), *The Dynamics of the Upper Ocean*, Cambridge Univ. Press, New York.

Stokes, G. G. (1847), On the theory of oscillatory waves, *Trans. Cambridge Philos. Soc.*, *8*, 441–455.

Støylen, E. (2008), Mass transport induced by internal Kelvin waves, Master's thesis, Univ. of Oslo, Oslo.

Tang, C. C. L., C. K. Ross, T. Yao, B. Petrie, B. M. DeTracey, and E. Dunlap (2004), The circulation, water masses and sea-ice of Baffin Bay, *Prog. Oceanogr.*, *63*(4), 183–228, doi:10.1016/j.pocean.2004.09.005.

Vlasenko, V., N. Stashchuk, K. Hutter, and K. Sabinin (2003), Nonlinear internal waves forced by tides near the critical latitude, *Deep Sea Res., Part I*, *50*, 317–338, doi:10.1016/S0967-0637(03)00018-9.

Weber, J. E. (1983), Steady wind- and wave-induced currents in the open ocean, *J. Phys. Oceanogr.*, *13*(3), 524–530, doi:10.1175/1520-0485(1983)013<0524:SWAWIC>2.0.CO;2.

Weber, J. E. (1987), Wave attenuation and wave drift in the marginal ice zone, *J. Phys. Oceanogr.*, *17*(12), 2351–2361, doi:10.1175/1520-0485(1987)017<2351:WAAWDI>2.0.CO;2.

Weber, J. E. H., G. Broström, and Ø. Saetra (2006), Eulerian versus Lagrangian approaches to the wave-induced transport in the upper ocean, *J. Phys. Oceanogr.*, *36*(11), 2106–2118, doi:10.1175/JPO2951.1.

Wunsch, C. (1973), On the mean drift in large lakes, *Limnol. Oceanogr.*, *18*(5), 793–795.

Wunsch, C. (1975), Internal tides in the ocean, *Rev. Geophys.*, *13*, 167–182, doi:10.1029/RG013i001p00167.

Xu, Z., and A. J. Bowen (1994), Wave- and wind-driven flow in water of finite depth, *J. Phys. Oceanogr.*, *24*(9), 1850–1866, doi:10.1175/1520-0485(1994)024<1850:WAWDFI>2.0.CO;2.

E. Støylen and J. E. H. Weber, Department of Geosciences, University of Oslo, PO Box 1022, Blindern, N-0315 Oslo, Norway. (eivind.stoylen@geo.uio.no)

II

Mean drift velocity in the Stokes interfacial edge wave

Jan Erik H. Weber[1] and Eivind Støylen[1]

Received 24 August 2010; revised 12 January 2011; accepted 20 January 2011; published 2 April 2011.

[1] The Stokes interfacial edge wave in a viscous rotating two-layer system is studied theoretically. The mean wave-induced Lagrangian drift velocity is obtained from the vertically integrated Eulerian equations of momentum and mass, correct to second order in wave steepness. The analysis is valid for shallow-water waves in the case when the upper layer is much thicker than the lower layer. In the lower layer the effect of viscosity is confined to a frictional boundary layer at the bottom. The waves are trapped by the bottom slope and can propagate in either direction along the bottom contours (in the y direction). Assuming that the waves attenuate in space as they propagate, this yields a Stokes drift velocity and a mean energy density E that decay exponentially in y. In this problem $-\partial E/\partial y$ is the relevant radiation stress forcing in the wave propagation direction. It is explained why this differs from the radiation-stress forcing of $-{}^3/_2\partial E/\partial y$ for plane waves in an unbounded nonrotating shallow ocean. The bottom stress acting on the mean Eulerian wave-induced flow is modeled by a turbulent friction coefficient. The results show that the maximum mean Eulerian drift current is considerably larger than the maximum Stokes drift velocity. Since the Eulerian current becomes negative at larger seaward distances, the total mean Lagrangian drift current is confined to a rather narrow wedge in the lower layer.

Citation: Weber, J. E. H., and E. Støylen (2011), Mean drift velocity in the Stokes interfacial edge wave, *J. Geophys. Res.*, *116*, C04002, doi:10.1029/2010JC006619.

1. Introduction

[2] Stokes' discovery of the surface edge wave [*Stokes*, 1880], did not receive much attention in the following years. In fact, nearly hundred years later one could find in the literature about edge waves: "It does not appear that the type of motion here referred to is very important" [*Lamb*, 1932, p. 447]. However, in recent years the interest in edge waves in homogeneous fluids has risen considerably. This is particularly so because they have been shown to be of fundamental importance in the dynamics and the sedimentology of the nearshore zone through their interaction with ocean swell and surf to produce rip current patterns, beach cusps and crescentic bars [*LeBlond and Mysak*, 1978]. The nonlinear mean mass transport in such waves has also been investigated, e.g., by *Weber and Ghaffari* [2009], where a comprehensive list of references to earlier works in a homogenous ocean can be found. The edge wave problem has also been carried on to a stratified ocean [*Greenspan*, 1970]. A thorough discussion of the linear edge wave problem in a rotating ocean with continuous stratification can be found in the work of *Llewellyn Smith* [2004].

[3] In the present study we consider an idealized two-layer situation where a thick fluid layer of constant density is on top of a much thinner layer of denser fluid. The bottom is sloping linearly, and the interface between the two fluids intersects the sloping bottom. This configuration is motivated by the observations of *Smith* [1976] from the Denmark Strait between Iceland and Greenland. The observations show a relatively thin bottom layer of dense water on the sloping Greenland side of the strait. In fact, similar bottom pools of dense bottom water, where the interface that separates them from the water above intersects the continental slope, may be found several places in the world's oceans; see, for example, the work of *Huhn et al.* [2008] for the location of the Weddell Sea bottom water near the shelf break in Antarctica. This situation is also common in the winter atmosphere when cold air near the ground is trapped by sloping terrain. In cases of little wind, this may lead to a stable inversion layer with an interface that intersects the mountain rise.

[4] It is obvious that the configuration described here can favor edge waves on the interface between the layers. Concerning the generation process, it is reasonable to assume an analogy between the Stokes surface edge wave and the present interfacial case. At the surface, observations demonstrate that high-frequency edge waves can occur when groups of incoming wind waves are breaking regularly at the beach, introducing a frequency that is smaller than that of the wind sea [*Huntley and Bowen*, 1973]. In the interior of the ocean internal solitary waves and wave trains are generated by the barotropic tide interacting with submarine topography, and they tend to break in the region where the thermocline intersects the shelf slope; see for

[1]Department of Geosciences, University of Oslo, Oslo, Norway.

0148-0227/11/2010JC006619

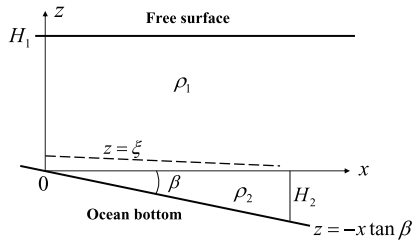

Figure 1. Sketch depicting the coordinate system used in the Eulerian description, with the interface and sloping bottom included. Here y is the coordinate along the isobaths, and the seaward direction is $x \to \infty$.

example the observation by *Apel et al.* [1985], or *Moum et al.* [2003]. The breaking process at the slope is also well captured by numerical modeling [e.g., *Vlasenko and Hutter*, 2002]. Analogous to the surface case, the intermittent process of interfacial wave breaking in the shoaling region may trigger an interfacial edge wave response. The corresponding wavelength will be given by the dispersion relation for the Stokes interfacial edge wave. Also, the generation of such waves in the deep ocean may be related to moving atmospheric pressure patterns [e.g., *Beardsley et al.*, 1977], forcing barotropic currents over ridges or canyons on the shelf slope.

[5] The purpose of the present study is to quantify the mean Lagrangian mass transport generated by the Stokes interfacial edge wave. In order to obtain a robust formulation, we consider the vertically integrated equations of momentum and mass [e.g., *Phillips*, 1977], and derive the mean Lagrangian mass flux to second order in wave steepness. This flow is potentially important for sediment transport. It is known from observations of breaking solitary waves in the shoaling region [*Moum et al.*, 2003], that this process generates turbulence, and hence leads to mixing of finer sediment in the water column. The derived wave-induced Lagrangian mean motion will therefore transport sediment in suspension along the isobaths away from the breaking solitary wave region, and thus contribute to the relocation of finer sediment and neutral tracers. However, it must be mentioned that the vertically averaged drift velocity here is obtained by dividing the volume flux by the local depth. In this way we do not resolve the motion in the bottom boundary layer, so this approach is not directed at the study of transport of heavy particles at the seabed.

[6] The rest of the paper is organized as follows. Section 2 defines the geometry of the model. It formulates the relevant mathematics of the problem, and derives the governing Eulerian equations for the depth-integrated mean motion. Section 3 studies the linear interfacial edge wave subject to friction in a thin bottom layer, and section 4 discusses the particular form of the radiation stress tensor in this problem. Section 5 derives an analytical solution for steady depth-integrated mean Eulerian velocity, correct to second order in wave steepness. The relevant physical parameters for this problem are addressed in section 6, and section 7 yields specific solutions for the mean drift currents. Finally, section 8 presents a short summary and some concluding remarks.

2. Mathematical Formulation

[7] We consider a two-layer system of homogeneous fluids of different densities ρ_1 and ρ_2 ($\rho_1 < \rho_2$). Trapped interfacial gravity waves may propagate along the interface between the two layers, where the lower layer has a linearly sloping bottom. The upper layer has a constant thickness H_1 in the two-layer region. We place the x axis at the undisturbed interface, and direct it into the semi-infinite sea, the y axis is along the bottom contours, and the z axis is vertically upward; see Figure 1. The velocity components are denoted by ($u_{1,2}$, $v_{1,2}$, $w_{1,2}$), and the pressure is $p_{1,2}$. The bottom shape is given by $z = -H_2 = -x \tan \beta$, where β is the sloping angle. The interface is situated at $z = \xi(x, y, t)$, where t is time. In this problem we assume that the upper layer is much thicker than the lower layer. We shall refer to flow parallel to the isobaths as along-slope flow, and normal to the isobaths as cross-slope flow.

[8] In the absence of viscosity and rotation, it is possible to find an exact solution in Lagrangian coordinates to this problem. Since the particle motion in edge waves occurs in planes parallel to the sloping bottom, we can apply the theory of plane Gerstner waves [*Gerstner*, 1809], e.g., following the work of *Constantin* [2001], for surface waves. When the upper layer is very thick, the analysis for the Stokes interfacial edge wave is analogous to that of *Constantin* [2001], replacing the acceleration due to gravity by the reduced gravity. As for the original Gerstner wave and the surface edge wave, the Stokes interfacial edge wave possesses vorticity in the direction normal to the bottom plane. Hence, it cannot be generated from rest by conservative forces, making this exact wave solution for an inviscid fluid less appealing from a physical point of view.

[9] When viscosity and the earth's rotation are taken into account, vorticity becomes inherent in the wave motion, but the Lagrangian analysis now becomes very cumbersome. In this case the calculations are most easily done in an Eulerian framework. Our main assumption will be that the waves are so long that we can make the hydrostatic approximation in the vertical. This is reasonable, since bottom slopes in the deep ocean usually are very small. Hence, within the trapping distance of the wave (~ one wavelength), the bottom layer will appear shallow. With a very deep upper layer, we can then apply a one-layer reduced gravity model [*McCreary*, 1976; *Busalacchi and O'Brien*, 1980] for this problem. However, we retain the nonlinear terms in the lower layer to capture the mean wave-induced mass flux.

[10] According to our adopted approach the velocity in the upper layer is negligible, so we skip the subscript 2 and denote the velocity in the lower layer as (u, v, w), etc. Furthermore, we denote periodic wave variables by a tilde, and the mean flow (averaged over the wave period) by an overbar. Mean horizontal volume fluxes in the lower layer ($\overline{U}$, $\overline{V}$) are defined by

$$\overline{U} = \overline{\int_{-H}^{\xi} u\,dz}, \quad \overline{V} = \overline{\int_{-H}^{\xi} v\,dz}, \tag{1}$$

where, in the shallow-water approximation, $H = \beta x$. These fluxes are actually the Lagrangian fluxes, since we integrate between material boundaries [*Phillips*, 1977; *Weber et al.*, 2006]. Integrating the governing equations in the vertical, and utilizing the full nonlinear boundary conditions at the interface and the sloping bottom, we obtain for the mean quantities in the lower layer, correct to second order in wave steepness [*Phillips*, 1977]:

$$\begin{aligned}
\frac{\partial \overline{U}}{\partial t} - f\overline{V} &= -g_* H\frac{\partial \overline{\xi}}{\partial x} + \frac{\overline{\tau}_i^{(x)}}{\rho} - \frac{\overline{\tau}_B^{(x)}}{\rho} - \frac{1}{2}g_*\frac{\partial}{\partial x}\overline{\tilde{\xi}^2} - \frac{\partial}{\partial x}\int_{-H}^{0}\overline{\tilde{u}^2}dz \\
&\quad - \frac{\partial}{\partial y}\int_{-H}^{0}\overline{\tilde{u}\tilde{v}}dz, \\
\frac{\partial \overline{V}}{\partial t} + f\overline{U} &= -g_* H\frac{\partial \overline{\xi}}{\partial y} + \frac{\overline{\tau}_i^{(y)}}{\rho} - \frac{\overline{\tau}_B^{(y)}}{\rho} - \frac{1}{2}g_*\frac{\partial}{\partial y}\overline{\tilde{\xi}^2} - \frac{\partial}{\partial x}\int_{-H}^{0}\overline{\tilde{u}\tilde{v}}dz \\
&\quad - \frac{\partial}{\partial y}\int_{-H}^{0}\overline{\tilde{v}^2}dz, \\
\frac{\partial \overline{\xi}}{\partial t} &= -\frac{\partial \overline{U}}{\partial x} - \frac{\partial \overline{V}}{\partial y}.
\end{aligned} \tag{2}$$

Here f is the constant Coriolis parameter, and g_* the reduced gravity defined as $g_* = g\Delta\rho/\rho$, where $\Delta\rho$ is the density difference between the lower and upper layer. Furthermore, $(\overline{\tau}_i^{(x)}, \overline{\tau}_i^{(y)})$ and $(\overline{\tau}_B^{(x)}, \overline{\tau}_B^{(y)})$ are the mean stress components at the interface and bottom, respectively.

3. The Linear Wavefield

[11] In this problem the oscillatory interfacial edge wave motion is influenced by viscosity. Since we consider shallow water, the viscous boundary layer at the bottom will dominate. Locally, the wave solution can be divided into a depth-independent part $\vec{\tilde{v}}_b$ and a viscous boundary layer part $\vec{\tilde{v}}_v$. The latter is only significant in a thin bottom layer of thickness δ. In the nonrotating case, $\delta = (2\nu/|\omega|)^{1/2}$, where ω is the wave frequency and ν the kinematic viscosity coefficient. When the wavefield is influenced by the earth's rotation, the bottom layer becomes more complicated [e.g., *Sverdrup*, 1927]. For Poincaré waves in a shallow unbounded ocean, in which the wave frequency is always larger than f, the dominating part of the boundary layer is associated with the anticyclonic component. The corresponding boundary layer thickness is $\delta = (2\nu/|\omega - f|)^{1/2}$. Here we study the Stokes interfacial edge wave, with a dispersion relation that is cubic in ω. We concentrate on the case where $\omega > f$. Then it easy to show that the cyclonic component of the wave motion vanishes identically, so $\delta = (2\nu/|\omega - f|)^{1/2}$ is the only boundary layer scale. Away from the origin, we assume that the local depth of the lower layer is much larger than boundary layer thickness, i.e., $H \gg \delta$. We are only interested in the depth-independent part of the wave solution, since this part dominates the contribution to the integrals in (2). It is easy to show that the effect of bottom friction will appear as a linear term in the equation for $\vec{\tilde{v}}_b$ [*Weber et al.*, 2009]. For a complex Fourier component, the friction term becomes $-(1 - i)r\vec{\tilde{v}}_b$. For the present problem with no-slip at the bottom, we find that

$$r = \frac{\nu^{1/2}|\omega - f|^{1/2}}{2^{1/2}H_m}, \tag{3}$$

where H_m is the mean depth of the lower layer in the region of wave trapping. We here assume that r is small, i.e., $r/\omega \ll 1$. Since the $ir\vec{\tilde{v}}_b$ part of the friction force is always much smaller than the acceleration term $-i\omega\vec{\tilde{v}}_b$, we can neglect it in the equations for the barotropic flow. From now on we only consider the depth-independent part of the wavefield, and we drop the subscript b. The governing linear equations become:

$$\begin{aligned}
\tilde{u}_t - f\tilde{v} + r\tilde{u} &= -g_*\xi_x, \\
\tilde{v}_t + f\tilde{u} + r\tilde{v} &= -g_*\xi_y, \\
\tilde{\xi}_t &= -(H\tilde{u})_x - (H\tilde{v})_y,
\end{aligned} \tag{4}$$

where subscripts denote partial differentiation. It is straight forward to eliminate $\tilde{u}$ and $\tilde{v}$ from this set of equations, and we get

$$L(\xi_t) = g_*\beta\big(M(\xi_x) + f\xi_y + xM\big(\xi_{xx} + \xi_{yy}\big)\big), \tag{5}$$

where the operators L and M are defined as:

$$M \equiv \frac{\partial}{\partial t} + r, \quad L \equiv \frac{\partial^2}{\partial t^2} + 2r\frac{\partial}{\partial t} + f^2, \tag{6}$$

omitting small r^2 terms. We look for the gravest (Stokes) interfacial edge wave mode, and assume that

$$\tilde{\xi} = \xi_0 \exp(-\kappa x + i(\kappa y - \omega t)), \tag{7}$$

where ξ_0 is the wave amplitude at the origin. Furthermore, ω is real, and

$$\kappa = k + i\alpha. \tag{8}$$

Here k is the real wave number and α is the (real) spatial damping rate. Insertion of (7) into (5) yields the complex dispersion relation

$$\omega^3 - \Big(f^2 + g_*k\beta\Big)\omega - fg_*k\beta + i\Big(g_*\beta(\omega\alpha + f\alpha + kr) - 2\omega^2 r\Big) = 0. \tag{9}$$

It can be shown [*LeBlond and Mysak*, 1978] that the real part of (9) can be factorized, yielding the three roots

$$\begin{aligned}
\omega_1 &= \frac{f}{2} + \left(\frac{f^2}{4} + \omega_0^2\right)^{1/2}, \\
\omega_2 &= \frac{f}{2} - \left(\frac{f^2}{4} + \omega_0^2\right)^{1/2}, \\
\omega_3 &= -f.
\end{aligned} \tag{10}$$

Here $\omega_0 = \pm(g_*k\beta)^{1/2}$ is the Stokes interfacial edge wave frequency for shallow-water waves in a nonrotating ocean. In the present problem we choose to study waves that are

propagating along the positive y axis with frequency larger than f, i.e., we take that $\omega = \omega_1$.

[12] The imaginary part of (9) yields

$$g_*\beta\alpha(\omega + f) = (2\omega^2 - \omega_0^2)r. \tag{11}$$

Utilizing that $\omega_0^2 = \omega_{1,2}^2 - f\omega_{1,2}$ from (10), we obtain for the spatial damping coefficient

$$\alpha = \frac{\omega r}{g_*\beta}. \tag{12}$$

Finally, from (4) and (7) we obtain for the real parts of the linear depth-independent wavefield:

$$\begin{aligned}
\tilde{\xi} &= \xi_0 \exp(-kx - \alpha y)\cos(-\alpha x + ky - \omega t),\\
\tilde{u} &= -\frac{\omega\xi_0}{\beta}\exp(-kx - \alpha y)\sin(-\alpha x + ky - \omega t),\\
\tilde{v} &= \frac{\omega\xi_0}{\beta}\exp(-kx - \alpha y)\cos(-\alpha x + ky - \omega t).
\end{aligned} \tag{13}$$

We note from this solution that frictional damping causes the lines of constant phase in the trapping region to tilt a small angle α/k with respect to the x axis. The potential wave maker in this problem is situated at $y = 0$, and the waves can in principle propagate in either direction, being attenuated as they progress (positive y: $\omega = \omega_1 > 0$, $\alpha > 0$, negative y: $\omega = \omega_2 < 0$, $\alpha < 0$).

4. The Radiation Stress Tensor

[13] Utilizing (13), it is trivial to calculate the wave-induced terms on the right-hand side of (2). Neglecting the interfacial friction in comparison with the much stronger bottom friction, the x and y components of the Lagrangian fluxes to second order in wave steepness then becomes

$$\begin{aligned}
\overline{U}_t - f\overline{V} + g_*H\overline{\xi}_x + \overline{\tau}_B^{(x)}/\rho &= -\frac{1}{2}g_*\left(\overline{\tilde{\xi}^2}\right)_x - \left(H\overline{\tilde{u}^2}\right)_x - \left(H\overline{\tilde{u}\tilde{v}}\right)_y = -S_{1x},\\
\overline{V}_t + f\overline{U} + g_*H\overline{\xi}_y + \overline{\tau}_B^{(y)}/\rho &= -\frac{1}{2}g_*\left(\overline{\tilde{\xi}^2}\right)_y - \left(H\overline{\tilde{u}\tilde{v}}\right)_x - \left(H\overline{\tilde{v}^2}\right)_y = -S_{2y}.
\end{aligned} \tag{14}$$

Here

$$S_1 = S_2 = \frac{(\omega_0^2 + 2kx\omega^2)}{4k\beta}\xi_0^2\exp(-2kx - 2\alpha y). \tag{15}$$

The quantity S can be related to the interfacial wave energy. We write the wave energy density E per unit length in the cross-slope direction for shallow water waves as

$$E = \frac{1}{2}\rho\left[H\left(\overline{\tilde{u}^2} + \overline{\tilde{v}^2}\right) + g_*\overline{\tilde{\xi}^2}\right], \tag{16}$$

where the contribution from the vertical velocity has been neglected. Insertion from (13) yields right away that

$$S_{1,2} = E/\rho. \tag{17}$$

For surface waves in an unbounded, nonrotating ocean it was demonstrated by *Longuet-Higgins and Stewart* [1960] that the time rate of change of the mean Lagrangian momentum flux in the wave direction (y direction) was forced by $-{}^1\!/_2\partial E/\partial y$ when the water was deep, and by $-{}^3\!/_2\partial E/\partial y$ when the water was shallow. In the present problem we note from (14) and (17) that the time rate of change of the along-shore mean Lagrangian momentum flux is forced by $-\partial E/\partial y$, which is in between the deep and shallow water values of *Longuet-Higgins and Stewart* [1960]. This should not come as a surprise, since the Stokes edge wave is different from that considered by *Longuet-Higgins and Stewart.* In particular, the velocity vector in progressive edge waves rotates in planes parallel to the sloping bottom, generating a $\tilde{u}$ component in the cross-wave direction. Now $\tilde{u}$ and $\tilde{v}$ are out of phase, so that does not affect the radiation stresses $S_{1,2}$ in (14), but it yields an additional contribution to the wave energy density (16).

[14] A striking parallel to this problem is the case of Poincaré waves in a rotating shallow ocean. In this case it is the effect of rotation that generates a horizontal velocity component in the cross-wave direction. For comparison we use the same configuration as in Figure 1, but now with a constant depth of the lower layer. Poincaré waves are solutions of the Klein-Gordon equation. For linear waves along the y axis, the solution is easily obtained from (4) for constant depth H:

$$\begin{aligned}
\tilde{\xi} &= \xi_0\exp(-\alpha y)\cos(ky - \omega t),\\
\tilde{u} &= -\frac{f\xi_0}{kH}\exp(-\alpha y)\left(\sin(ky - \omega t) - \left(\frac{\alpha}{k} + \frac{r}{\omega}\right)\cos(ky - \omega t)\right),\\
\tilde{v} &= \frac{\omega\xi_0}{kH}\exp(-\alpha y)\left(\cos(ky - \omega t) + \frac{\alpha}{k}\sin(ky - \omega t)\right).
\end{aligned} \tag{18}$$

Here $\omega^2 = f^2 + g_*Hk^2$, and $\alpha = (\omega^2 + f^2)r/(2g_*Hk\omega)$. From (16) we readily find for the energy density that

$$E = \frac{\rho\omega^2\xi_0^2}{2k^2H}\exp(-2\alpha y). \tag{19}$$

The wave forcing terms are the same as in (14). Applying (18), we obtain that $S_1 = 0$, while

$$S_2 = \frac{1}{2}\left(3 - \frac{f^2}{\omega^2}\right)\frac{\omega^2\xi_0^2}{2k^2H}\exp(-2\alpha y) = \frac{1}{2}\left(3 - \frac{f^2}{\omega^2}\right)\frac{E}{\rho}. \tag{20}$$

Since $|\omega| > f$ for Poincaré waves, we always have that $S_2 < 3E/2\rho$ for this shallow water problem.

[15] For edge waves the effect of the earth's rotation is not really needed to yield a horizontal cross-wave velocity component and a deviation from the form of the *Longuet-Higgins and Stewart*'s radiation stress tensor. It is the effect of the sloping bottom that is the crucial factor. This is easily seen from the one-layer case studied by *Weber and Ghaffari* [2009]. They considered the Stokes surface edge wave for arbitrary bottom slope in a nonrotating fluid, and calculated the total wave energy density $\langle E\rangle$ by integrating horizontally over the trapped region. They found that the integrated radiation stress component $\langle S_2\rangle$ was given by $\langle S_2\rangle = \langle E/\rho\rangle$ for all slope angles (their equation (18)).

5. The Steady Transport

[16] We consider steady mean flow. The continuity equation in (2) then yields $O(\overline{U}) \sim O(\alpha\overline{V}/k)$, which means

that $|\overline{U}| \ll |\overline{V}|$. Accordingly, the mean velocity in the x direction is small. Since the turbulent bottom friction in this direction is taken to be proportional to the mean velocity (see the discussion below), it is also small, and can be neglected in comparison with the mean pressure gradient and the radiation stress component. Hence, the steady Lagrangian fluxes are governed by

$$\begin{aligned} -f\overline{V} + g_* \beta x \overline{\xi}_x &= -S_x, \\ f\overline{U} + g_* \beta x \overline{\xi}_y &= -S_y - T, \\ \overline{U}_x + \overline{V}_y &= 0, \end{aligned} \tag{21}$$

where $T = \overline{\tau}_B^{(y)}/\rho$, and $S = S_1 = S_2$. In (21) we have that $\overline{V} = \overline{V}_E + \overline{V}_S$, where $\overline{V}_E$ is the mean Eulerian flux, and $\overline{V}_S$ is the Stokes flux [*Stokes*, 1847]. From (13) we readily obtain the Stokes drift velocity $(\overline{u}_S, \overline{v}_S)$ [e.g., *Longuet-Higgins*, 1953]:

$$\overline{u}_S = 0, \quad \overline{v}_S = \frac{\omega k \xi_0^2}{\beta^2} \exp(-2kx - 2\alpha y) \tag{22}$$

The along-slope Stokes flux in our case then becomes

$$\overline{V}_S = \beta x \overline{v}_S = \frac{k\omega\xi_0^2}{\beta} x \exp(-2kx - 2\alpha y). \tag{23}$$

By operating the curl on (21), we readily find that

$$g_* \beta \overline{\xi}_y = -T_x. \tag{24}$$

Often bottom friction acting on the turbulent mean flow is modeled as the square of the velocity times a bottom drag coefficient c_D. For simplicity, we here assume a linear bottom friction. The relation between the linear friction coefficient K and c_D can be approximated as $K = c_D v_B$, where v_B is a typical near-bottom mean velocity [*Gjevik et al.*, 1994; *Nøst*, 1994]. Accordingly,

$$T = K\overline{v}_E, \tag{25}$$

where $\overline{v}_E = \overline{V}_E/(\beta x)$. It is worth noting that we by this procedure separate the effect of friction on the wavefield from the effect of friction on the mean flow, which is physically sound [*Jenkins*, 1989; *Weber and Melsom*, 1993; *Ardhuin and Jenkins*, 2006].

[17] Assuming that $\overline{\xi}$, $\overline{v}_E \propto \exp(-2\alpha y)$, we find from the x component of (21), and (23) and (24), that

$$x\overline{v}_{Exx} - \frac{2\alpha f\beta}{K} x\overline{v}_E = -\frac{2\alpha}{K}\left(S_x - f\overline{V}_S\right). \tag{26}$$

Obviously, for trapped waves we must have

$$\overline{v}_E \to 0, \quad x \to \infty. \tag{27}$$

Furthermore, from the y component of (21), we obtain, using (25):

$$\overline{v}_E = \frac{\alpha g_* \xi_0^2}{2K} \exp(-2\alpha y), \quad x = 0. \tag{28}$$

We note that in this problem $1/(2k)$ is a typical length scale, and $v_0 = \alpha g_* \xi_0^2/(2K)$ is a typical mean velocity scale. Non-dimensional lengths can then be written $X = 2kx$, $Y = 2ky$, while the dimensionless along-slope mean Eulerian velocity q_E can be defined by

$$\overline{v}_E = v_0 \exp(-\alpha Y/k) q_E(X). \tag{29}$$

Then (26) becomes

$$X\frac{d^2 q_E}{dX^2} - G^2 X q_E = A(BX - 1)\exp(-X), \tag{30}$$

subject to

$$\begin{aligned} q_E &= 1, \quad X = 0, \\ q_E &\to 0, \quad X \to \infty. \end{aligned} \tag{31}$$

In (30) the dimensionless parameters are

$$A = \frac{f\omega}{\omega_0^2}, \quad B = \frac{\omega + f}{f}, \quad G = \left(\frac{\alpha f \beta}{2k^2 K}\right)^{1/2}. \tag{32}$$

An analytical solution of (30) can be found in terms of exponential integrals. Considering nonzero values of X, (30) becomes

$$\frac{d^2 q_E}{dX^2} - G^2 q_E = A(B - 1/X)\exp(-X), \tag{33}$$

which may be solved by utilizing the variation of parameters method. Since G is a positive constant, the complementary part of the solution $q^{(C)}$ is readily obtained:

$$q^{(C)} = D_1 \exp(GX) + D_2 \exp(-GX), \tag{34}$$

where D_1, D_2 are constants. The particular solution $q^{(P)}$ may be written

$$q^{(P)} = m_1(X)\exp(GX) + m_2(X)\exp(-GX), \tag{35}$$

for some functions m_1, m_2, subject to the conditions

$$\begin{aligned} &m_1'(X)\exp(GX) + m_2'(X)\exp(-GX) = 0 \\ &Gm_1'(X)\exp(GX) - Gm_2'(X)\exp(-GX) = A(B - 1/X)\exp(-X). \end{aligned} \tag{36}$$

Here primes denote differentiation.

[18] The solution of (36) is obtained using exponential integrals [*Abramowitz and Stegun*, 1972], defined as

$$Ei(X) = \int_{-\infty}^{X} \frac{e^t}{t} dt. \tag{37}$$

This function is singular at $X = 0$, and actual values for nonzero X must be obtained by numerical evaluation. The expressions for m_1, m_2 are, when $G \neq 1$:

$$\begin{aligned} m_1 &= -\frac{A}{2G}\left[\frac{B}{(G+1)} e^{-(G+1)X} + Ei(-(G+1)X)\right], \\ m_2 &= -\frac{A}{2G}\left[\frac{B}{(G-1)} e^{(G-1)X} - Ei((G-1)X)\right]. \end{aligned} \tag{38}$$

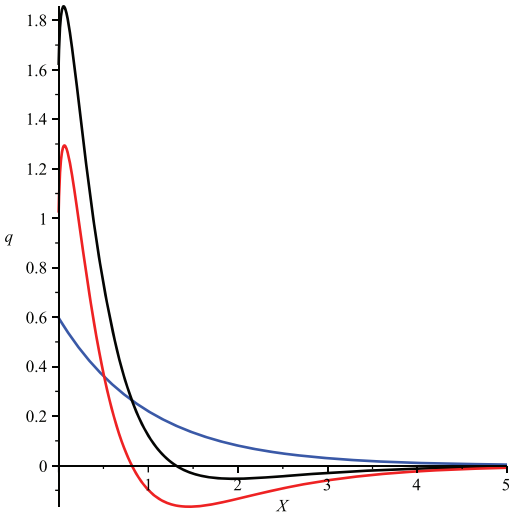

Figure 2. Nondimensional mean velocity q as function of nondimensional seaward distance X for interfacial edge waves with $\lambda = 60$ km (period 12.3 h). Blue curve indicates Stokes drift velocity q_S, red curve indicates Eulerian mean current q_E, and black curve indicates Lagrangian mean drift current q_L.

For the special case $G = 1$, m_1 becomes unaltered, but now

$$m_2 = -\frac{A}{2}(BX - \ln X). \tag{39}$$

For large X, $q^{(P)}$ approaches zero. In the limit $X \to 0^+$, the parts of $Ei(-(G+1)X)$ and $Ei((G-1)X)$ that grows without limit do cancel, yielding a finite value for $q^{(P)}$. To satisfy the boundary conditions (31), we then take

$$D_1 = 0, \quad D_2 = 1 - \lim_{X \to 0^+} q^{(P)}. \tag{40}$$

Inserting from (38) and (40) into (34) and (35), the complete dimensionless Eulerian mean velocity becomes

$$q_E = q^{(C)} + q^{(P)}. \tag{41}$$

It is also straight forward to solve (30) numerically. We realize that very close to $X = 0$, the solution can be approximated as

$$q_E = 1 - AX \ln X. \tag{42}$$

This implies that

$$\frac{dq_E}{dX} = -A(\ln X + 1), \tag{43}$$

for very small X. Equation (30) is then readily solved numerically for the coupled system of the two variables q_E and dq_E/dX by utilizing (42) and (43), when X very close to zero, to obtain starting values in a traditional numerical shooting procedure.

[19] Analogous to (29) we can define a dimensionless Stokes drift velocity q_S from (22) by

$$\bar{v}_S = v_0 \exp(-\alpha Y/k) q_S(X). \tag{44}$$

The dimensionless vertically averaged Lagrangian drift velocity along the slope then becomes

$$q_L = q_E + q_S. \tag{45}$$

Before we discuss specific solutions of this problem, we need to assess the values of the relevant physical parameters. This will be done in section 6.

6. Physical Parameters

[20] By specifying the eddy viscosity ν that acts to dampen the linear wavefield, we obtain the friction coefficient r and the spatial wave attenuation coefficient α from (3) and (12), for a prescribed wavelength. As explained in section 5, the relation between the linear friction coefficient K and the drag coefficient c_D for the mean flow can be approximated as $K = c_D v_B$, where v_B is a typical near-bottom mean velocity [*Gjevik et al.*, 1994; *Nøst*, 1994]. With typical values $c_D \sim 10^{-3}$, and $v_B \sim 10^{-2}$ m s^{-1}, we obtain that $K \sim 10^{-5}$ m s^{-1} in this problem. For the modeling of tidal currents in the Barents Sea a characteristic value of the eddy viscosity is $\nu \sim 10^{-3}$ m^2 s^{-1} [*Nøst*, 1994]. For surface waves at a sloping beach, eddy viscosity estimates are higher by a factor of 10 to 50 [*Apotsos et al.*, 2007], mainly because of turbulence induced by wave breaking. At a gently sloping bottom in the deep ocean we expect the turbulence level to be about one order of magnitude smaller than for the surface case, and we use the tidal value $\nu \sim 10^{-3}$ m^2 s^{-1} in quantifying the drift induced by the Stokes interfacial edge wave. From ocean data [*Smith*, 1976] it seems reasonable to assume $\beta = 0.01$ for the bottom slope, and $g_* = 3 \times 10^{-3}$ m s^{-2} for the reduced gravity. The value of the Coriolis parameter is taken to be $f = 1.2 \times 10^{-4}$ s^{-1}.

[21] The value of the drift current in this problem also depends on the wavelength and the wave amplitude. To assess a reasonable wavelength, we consider a possible forcing either by a moving atmospheric front, or the barotropic tide. When looking at our dispersion relation (10), we find that for a wavelength $\lambda = 60$ km, together with the assessed values of β and g_*, the corresponding wave period will be a little more than 12 h. Hence, this length scale could be imposed on our system by a narrow passing front, or the semidiurnal tide. The relevant mean depth must be related to the dimension of the wave trapping region. Since the Stokes interfacial wave practically vanishes outside $x = \lambda$, we take that $H_m = \beta\lambda/2$ in this problem.

[22] Shorter scales may be related to breaking of internal solitary waves at the bottom slope. For example, as observed by *Apel et al.* [1985], packets of solitons separated by a typical distance of 100 km, were generated by the barotropic tide interacting with bottom topography in the Sulu Sea. With a phase speed of 2.5 m s^{-2}, this would mean that soliton packets could break at the slope with about 10 h intervals. In our case, this time scale would excite interfacial edge waves with wavelength of about 20 km.

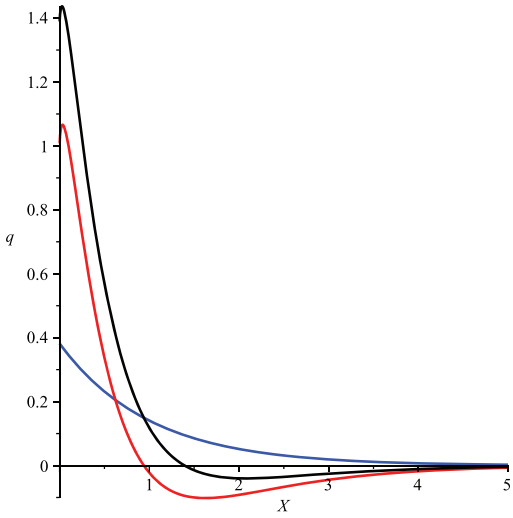

Figure 3. Same as in Figure 2 but for λ = 20 km (period 10 h).

[23] Because of lack of observational evidence, the amplitude of the interfacial wave is difficult to assess. However, because of the small density difference between the upper and lower layer, and the fact that the lower layer typically is 150–300 m thick, it is not unreasonable to assume that we have interfacial amplitudes in the range of 1 to 20 m. In fact, for interfacial waves in the upper ocean, it is not uncommon to find amplitudes that are about 10 percent of the upper layer thickness. For internal waves in a continuously stratified ocean, amplitudes of 100 m and more are reported [see *Vlasenko et al.*, 2005, and references therein]. Since the wave amplitude depends on the forcing mechanisms (barotropic tides, atmospheric disturbances), which are not so well known for bottom layers, we here adopt a conservative estimate of 7 m for the interfacial wave amplitude.

7. Results for the Depth-Averaged Mean Drift

[24] Utilizing the physical parameters listed in section 6, we can calculate the Stokes drift velocity and the mean Eulerian drift current from the formulae in section 6, and hence determine the dimensionless Lagrangian drift current from (45). In Figure 2 we have depicted q_S, q_E, and q_L as function of nondimensional seaward distance when the wavelength is 60 km. We note that q_E is negative for $X >$ 0.8, while Stokes drift velocity q_S is always positive. The Eulerian part of the total drift dominates the Stokes drift in this example. However, because of the negative values of the Eulerian current at larger X, the Lagrangian drift is basically confined to the region $X < 1.3$, or dimensionally $x < 6.2$ km, in this example.

[25] For smaller scales, typically 20 km, as discussed in section 5, the induced mean velocities become larger. The result is plotted in Figure 3 for the same physical parameters as before. Also in this example the Eulerian current is considerably larger than the Stokes drift, but because of the negative values of q_E for larger X, the mean Lagrangian drift is basically confined to the region $X < 1.5$ (dimensionally, $x < 2.4$ km). The velocity scale v_0 in (29) for the two examples considered here was 1.2 cm s^{-1} and 7 cm s^{-1}, respectively. This yields maximum dimensional drift velocities of 2.2 cm s^{-1} and 10 cm s^{-1} in Figures 2 and 3.

[26] Finally, from the parameters used in these two examples, we find that the thickness of the viscous bottom boundary layer, $\delta = (2\nu/(\omega - f))^{1/2}$, was 9.5 and 4.7 m, while the mean depth $H_m = \beta\lambda/2$ are 150 and 100 m, respectively. Hence, the assumption $\delta/H_m \ll 1$ holds well for both cases.

8. Summary and Concluding Remarks

[27] For surface waves in an unbounded nonrotating ocean it was demonstrated by *Longuet-Higgins and Stewart* [1960] that the time rate of change of the mean Lagrangian momentum flux in the wave direction (y direction) was forced by $-{}^1\!/_2 \partial E/\partial y$ when the water was deep, and by $-{}^3\!/_2 \partial E/\partial y$ when the water was shallow. In the present problem of the Stokes interfacial edge wave in shallow water, we note from (14) and (17) that the time rate of change of the along-shore mean Lagrangian momentum flux is forced by $-\partial E/\partial y$. It is explained that this difference is basically due to the cross-wave horizontal motion in edge waves induced by the sloping bottom.

[28] The main aim of this paper has been to quantify the difference between the Stokes drift velocity and the mean Eulerian drift current in their contribution to the mean Lagrangian drift in the Stokes interfacial edge wave. We have considered this difference for two possible wavelengths. For long waves, with frequencies close to the semidiurnal tide, the maximum mean Eulerian drift current is about twice as large as the Stokes drift. For shorter wavelengths, which may be related to the forcing by breaking internal solitary waves, the Stokes drift velocity increases, but it is still considerably smaller than the mean Eulerian current. In both cases, one important difference between the Eulerian and Stokes contributions is that the Eulerian current changes sign and becomes negative at larger seaward distances. As a result, the Lagrangian drift is confined to a narrow wedge in the lower layer.

[29] In conclusion, we think that the wave-induced mean drift velocity discussed here may be of importance for the net transport along the deep shelf of neutral tracers, pollutants, as well as light sediments in suspension.

References

Abramowitz, A., and I. A. Stegun (Eds.) (1972), *Handbook of Mathematical Functions With Formulas, Graphs, and Mathematical Tables*, *Appl. Math. Ser.*, vol. 55, 10th ed., Natl. Bur. of Stand., Washington, D. C.

Apel, J. R., J. R. Holbrook, A. K. Liu, and J. J. Tsai (1985), The Sulu Sea internal soliton experiment, *J. Phys. Oceanogr.*, *15*, 1625–1651, doi:10.1175/1520-0485(1985)015<1625:TSSISE>2.0.CO;2.

Apotsos, A., B. Raubenheimer, S. Elgar, R. T. Guza, and J. A. Smith (2007), Effects of wave rollers and bottom stress on wave setup, *J. Geophys. Res.*, *112*, C02003, doi:10.1029/2006JC003549.

Ardhuin, F., and A. D. Jenkins (2006), On the interaction of surface waves and upper ocean turbulence, *J. Phys. Oceanogr.*, *36*, 551–557, doi:10.1175/JPO2862.1.

Beardsley, R. C., H. Mofjeld, M. Wimbush, C. N. Flagg, and J. A. Vermersch Jr. (1977), Ocean tides and weather-induced bottom pressure fluctuations in the Middle-Atlantic Bight, *J. Geophys. Res.*, *82*, 3175–3182, doi:10.1029/JC082i021p03175.

Busalacchi, A. J., and J. J. O'Brien (1980), The seasonal variability in a model of the tropical Pacific, *J. Phys. Oceanogr.*, *10*, 1929–1951.
Constantin, A. (2001), Edge waves along a sloping beach, *J. Phys. A Math. Gen.*, *34*, 9723–9731, doi:10.1088/0305-4470/34/45/311.
Gerstner, F. (1809), Theorie der wellen samt einer daraus abgeleiteten theorie der deichprofile, *Ann. Phys.*, *2*, 412–455.
Gjevik, B., E. Nøst, and T. Straume (1994), Model simulations of the tides in the Barents Sea, *J. Geophys. Res.*, *99*, 3337–3350, doi:10.1029/93JC02743.
Greenspan, H. P. (1970), A note on edge waves in a stratified fluid, *Stud. Appl. Math.*, *49*, 381–388.
Huhn, O., H. H. Hellmer, M. Rhein, C. Rodehacke, W. Roether, M. P. Schodlok, and M. Schröder (2008), Evidence of deep- and bottom-water formation in the western Weddell Sea, *Deep Sea Res. Part II*, *55*, 1098–1116, doi:10.1016/j.dsr2.2007.12.015.
Huntley, D. A., and A. J. Bowen (1973), Field observations of edge waves, *Nature*, *243*, 160–162, doi:10.1038/243160a0.
Jenkins, A. D. (1989), The use of a wave prediction model for driving a near-surface current model, *Ocean Dyn.*, *42*, 133–149, doi:10.1007/BF02226291.
Lamb, S. H. (1932), *Hydrodynamics*, Cambridge Univ. Press, U. K.
LeBlond, P. H., and L. A. Mysak (1978), *Waves in the Ocean*, Elsevier, Amsterdam.
Llewellyn Smith, S. G. (2004), Stratified rotating edge waves, *J. Fluid Mech.*, *498*, 161–170, doi:10.1017/S002211200300702X.
Longuet-Higgins, M. S. (1953), Mass transport in water waves, *Philos. Trans. R. Soc. London A*, *245*, 535–581, doi:10.1098/rsta.1953.0006.
Longuet-Higgins, M. S., and R. W. Stewart (1960), Changes in the form of short gravity waves on long waves and tidal currents, *J. Fluid Mech.*, *8*, 565–583, doi:10.1017/S0022112060000803.
McCreary, J. (1976), Eastern tropical ocean response to changing wind systems: With application to El Niño, *J. Phys. Oceanogr.*, *6*, 632–645, doi:10.1175/1520-0485(1976)006<0632:ETORTC>2.0.CO;2.
Moum, J. N., D. M. Farmer, W. D. Smyth, L. Armi, and S. Vagle (2003), Structure and generation of turbulence at interfaces strained by internal solitary waves propagating over the continental shelf, *J. Phys. Oceanogr.*, *33*, 2093–2112, doi:10.1175/1520-0485(2003)033<2093:SAGOTA>2.0.CO;2.
Nøst, E. (1994), Calculating tidal current profiles from vertically integrated models near the critical latitude in the Barents Sea, *J. Geophys. Res.*, *99*, 7885–7901, doi:10.1029/93JC03485.
Phillips, O. M. (1977), *The Dynamics of the Upper Ocean*, Cambridge Univ. Press, Cambridge, U. K.
Smith, P. C. (1976), Baroclinic instability in the Denmark Strait Overflow, *J. Phys. Oceanogr.*, *6*, 355–371, doi:10.1175/1520-0485(1976)006<0355:BIITDS>2.0.CO;2.
Stokes, G. G. (1847), On the theory of oscillatory waves, *Trans. Cambridge Philos. Soc.*, *8*, 441–455.
Stokes, G. G. (1880), Report on recent researches in hydrodynamics, in *Papers*, vol. 1, pp. 157–187, Cambridge Univ. Press, Cambridge U. K.
Sverdrup, H. U. (1927), Dynamics of the tides on the North Siberian shelf: Results from the Maud Expedition, *Geophys. Norw.*, *4*(5), 1–75.
Vlasenko, V., and K. Hutter (2002), Numerical experiments on the breaking of solitary internal waves over a slope-shelf topography, *J. Phys. Oceanogr.*, *32*, 1779–1793, doi:10.1175/1520-0485(2002)032<1779:NEOTBO>2.0.CO;2.
Vlasenko, V., N. Stashchuk, and K. Hutter (2005), *Baroclinic Tides: Theoretical Modeling and Observational Evidence*, 372 pp., doi:10.1017/CBO9780511535932, Cambridge Univ. Press, U. K.
Weber, J. E. H., and P. Ghaffari (2009), Mass transport in the Stokes edge wave, *J. Mar. Res.*, *67*, 213–224, doi:10.1357/002224009789051182.
Weber, J. E., and A. Melsom (1993), Transient ocean currents induced by wind and growing waves, *J. Phys. Oceanogr.*, *23*, 193–206, doi:10.1175/1520-0485(1993)023<0193:TOCIBW>2.0.CO;2.
Weber, J. E. H., G. Broström, and Ø. Saetra (2006), Eulerian versus Lagrangian approaches to the wave-induced transport in the upper ocean, *J. Phys. Oceanogr.*, *36*, 2106–2118, doi:10.1175/JPO2951.1.
Weber, J. E. H., K. H. Christensen, and C. Denamiel (2009), Wave-induced setup of the mean surface over a sloping beach, *Cont. Shelf Res.*, *29*, 1448–1453, doi:10.1016/j.csr.2009.03.010.

E. Støylen and J. E. H. Weber, Department of Geosciences, University of Oslo, PO Box 1022, Blindern, N-0315 Oslo, Norway. (j.e.weber@geo.uio.no)

III

Tidally induced internal motion in an Arctic fjord

Eivind Støylen

Department of Geosciences, University of Oslo, Norway

Abstract

The internal response in a stratified partially enclosed basin subject to tidal forcing through a narrow entrance is investigated. Applying a non-linear 3D numerical model in an idealized topography, we study the generation and propagation of tidally induced internal Kelvin waves, when conditions through the entrance are baroclinically sub- or supercritical. We then move to a realistic topography of Van Mijenfjorden in Svalbard, where model results are compared to time series measurements performed in August 2010. Results from both the model and measurements indicate the presence of internal Kelvin waves, even when conditions through the entrance are supercritical. The entrance of Van Mijenfjorden is split in two sounds. Closing each sound separately reveals that internal Kelvin waves are generated at both sounds. However, higher resolution and better topography representation is needed to accurately describe the influence of the southern sound.

1. Introduction

Internal waves in the Arctic region have received increasing scientific interest in the later years. The Yermak Platau is noted as an important region for enhanced internal wave activity [e.g. *Padman and Dillon*, 1991; *Fer et al.*, 2010]. Wind induced internal waves are important in seasonally ice covered regions, as demonstrated in the Northern Chuckchi Sea by *Rainville and Woodgate* [2009]. In Arctic fjords short period internal waves are observed under ice [*Marchenko et al.*, 2010; *Morozov and Marchenko*, 2012], and larger internal Kelvin waves are documented in Kongsfjorden-Krossfjorden system [*Svendsen et al.*, 2002].

Internal waves in fjords are typically forced by changing winds and the barotropic tide. For fjords that are wide with respect to the internal Rossby radius, one part of the internal wave field may arise as internal Kelvin waves propagating cyclonically around the fjord. Such waves induce a mean current in the wave propagation direction [*Støylen and Weber*, 2010], which may lead to accumulation or deposition of pollutants and biological material in certain areas along the coastline. As discussed in *Cottier et al.* [2010] fjords in the Arctic are typically wide with respect to the baroclinic Rossby radius, thus internal Kelvin waves are to be expected in many stratified Arctic fjords given sufficient forcing.

In the present work we consider a particular wide Arctic fjord, namely Van Mijenfjorden in Svalbard. The entrance of this fjord is partly covered by an island, which restricts water inflow to two narrow sounds and thus makes the fjord a good "laboratory fjord" for process studies [e.g. *Widell et al.*, 2006; *Fer and Widell*, 2007]. Our aim is to describe the generation and propagation of internal waves induced by tides in this fjord, by use of CTD-measurements and a 3D numerical model. In particular we investigate the possibilities of internal Kelvin waves, as suggested in *Støylen and Weber* [2010] and *Skarðhamar and Svendsen* [2010]. The sensitivity of internal wave generation to hydraulic conditions through the fjord entrance is investigated

numerically. Finally, as the fjord entrance consists of two sounds we demonstrate numerically the effect of closing each sound on the respective wave field.

This study is organized as follows: In section 2 we present some theoretical background for internal waves in Arctic fjords. Measurement data from Van Mijenfjorden is shown in section 3. In section 4 we treat the numerical problem in an idealized geometry, before applying a realistic topography of Van Mijenfjorden in section 5. Finally we discuss our findings and provide concluding remarks in section 6.

2. Theory

In this section we briefly discuss what types of internal motion we may expect in an Arctic fjord, and describe basic theory regarding the internal Kelvin wave. Where appropriate, we will assume a two-layer system with constant densities ρ_1 and ρ_2 for the upper and lower layer, respectively. Other variables have similar subscripts. The Cartesian coordinate system (x,y,z) with z as upward vertical direction has corresponding current components (u,v,w).

Internal waves span a broad range of spatial and temporal scales. In a fjord basin there may be propagating Poincaré waves [*Brown*, 1973; *Farmer and Freeland*, 1983] and soliton trains [*Helfrich and Melville*, 2006]. Along the coast there may possibly be propagating edge waves [*Llewellyn Smith*, 2004; *Weber and Støylen*, 2011] trapped by the sloping bottom, or the internal Kelvin wave trapped by rotation. The latter is discussed in more detail below.

There are several mechanisms for internal wave generation. In an Arctic fjord the dominant sources of forcing are changing wind fields, and the barotropic tide interacting with topographic features at the fjord entrance. We will restrict our attention to the tidal case. When the cross sectional area of the fjord entrance is narrow, as is the case in Van Mijenfjorden, the tidal current is intensified here. If the water is stratified, one can determine whether conditions are sub- or supercritical with respect to the first baroclinic mode. For a two-layer system a

densimetric Froude number $F_D = |u_s|/c_i$ is defined, where c_i is the baroclinic phase velocity and u_s is the upper layer current. $F_D < 1$ indicates subcritical conditions, which favors generation of long internal waves. When $F_D > 1$, the current enters the fjord as a jet, and there will be a hydraulic jump just inside the entrance. Now the generation of long waves is prohibited, according to *Stigebrandt* [1980]. He notes that for weakly supercritical conditions there could still be wave generation. This is indeed observed in Loch Etive, Scotland [*Inall et al.*, 2004; *Stashchuk et al.*, 2007], which is a typical "jet-type" fjord following the definition from *Stigebrandt and Aure* [1989]. We conclude that tidally forced internal waves should be present in a wide range of fjords with proper stratification.

If the fjord width is large compared to the baroclinic Rossby radius $a = c_i / f$, wave solutions of Kelvin type may exist. Here f is the Coriolis parameter, $c_i = (g' H_1)^{1/2}$ and $g' = g(\rho_2 - \rho_1)/\rho_2$ for a system with deep lower layer and upper layer thickness H_1. Following the derivation in *Støylen and Weber* [2010] we consider forcing of sine-type oscillation, and for the sake of simplicity we neglect friction here. Then, for a wave travelling along the *x*-axis on the interface ξ between the upper and lower layer:

$$\xi = \xi_0 e^{-y/a} \cos(kx - \omega t) \qquad (1)$$

Here we have the coast at $y = 0$ and ocean at $y > 0$. Furthermore ξ_0, ω and k are wave amplitude, wave number and frequency, respectively. The interface displacement is largest near the coast, and is exponentially damped seaward. The frequency is the forcing frequency; in our case the M_2 tidal component.

Linear wave solutions for free internal Poincaré waves are restricted by the critical latitude for the respective forcing frequency, which for the M_2 tidal component is $\varphi = 74.5°$ [*V. Vlasenko et al.*, 2003]. This restriction does not apply to internal Kelvin waves, and they may exist in Arctic regions above the critical latitude [*Farmer and Freeland*, 1983].

3. Field work

Our study site is Van Mijenfjorden in Svalbard, see Figure 1. This fjord is an interesting "laboratory fjord" for the study of propagating baroclinic waves of tidal periodicity. At the outer region of the fjord the near-coast bathymetry is quite steep. The entrance of the fjord is partly covered by an island, Akseløya. This restricts the water exchange to two narrow sounds, Akselsundet in the north, and Mariasundet in the south. The typical tidal amplitude outside Akseløya is in the range from 0.3 m to 0.8 m (see Figure 2), and currents measured in Akselsundet may exceed 2 m s^{-1} [*Bergh*, 2004]. During summer and autumn the water in the fjord is stratified due to glacial melting. It is during this period we expect baroclinic tidal activity to be most pronounced. Indeed, *Skarðhamar and Svendsen* [2010] report a 22 hour CTD-time series near Blixodden in July 1996. They observe a displacement of the pycnocline of 20 m, which they argue may be caused by a passing internal Kelvin wave.

Our measurements were performed in the period 9.-14. August 2010 during a cruise with RV *Håkon Mosby*. Data was collected using a conventional CTD with up- and down looking LADCP (Lowered Acoustic Doppler Current Profiler) instruments attached. Weather data was collected on the ship. Figure 1 shows a map of the measurement locations; see also Table 1. Labels A-D denote horizontal sections, and TS1-TS6 are time series. For each time series station, a sample was obtained approximately every 30 minutes for a period of 13 hours, thus encompassing the M_2 tidal period of 12.4 hours. The location of the stations were chosen as to best capture a potentially propagating internal Kelvin wave, which is expected to have its largest amplitude near the coast (see section 2), and propagating cyclonically around the basin.

A general view of the hydrography of the basin is presented in Figure 3 a)-f). We notice a distinctive stratification, as is expected in this season. Surface water is relatively fresh due to runoff from glaciers, and warmer than the water below due to surface heating; see Figure 2 for

air temperature measurements. From Figure 3 a) we notice the colder and saltier deep water originating from outside the fjord. During high tide this water is lifted over the sill as can be inferred from the D-section; the outmost D-profile was the last sample in the section, and was thus captured during high tide; see Figure 2. The repeated sections B and C, Figure 3 c)-f), indicate a strong variability on relatively short time scales throughout the entire fjord basin. This is in accordance with *Skarðhamar and Svendsen* [2010], where a more detailed description of the short-term hydrographic variability in Van Mijenfjorden can be found. In the present work we restrict our attention to the possible internal waves trapped near coast.

Plots of velocity and density for each time series station are presented in Figure 4. Again we refer to Figure 2 for comparison with the tide. Outside Akseløya (TS1) the dominant features of the tide entering and leaving Akselsundet are distinguishable in the upper 40 meters. Just inside Akselsundet (TS2) we observe intense mixing associated with tidal inflow. This is presumably a hydraulic jump due to the high in-flow velocities at mid-straight as mentioned above. Further south along Akseløya north of Mariasundet (TS3) the flow field is dominated by a southgoing current generated just inside Akselsundet. Assuming a velocity of 35 cm s^{-1} and a distance of 7.5 km, we obtain a travel time of about 6 hours, which agrees with the time of tidal inflow inside Akselsundet. We note the displacements of the isopycnals which weakly indicate oscillations of tidal periodicity. Along the southern coast (TS4) the currents are in-fjord during the entire tidal period. This station is potentially influenced by inflow at both sounds, thus a more complicated current structure is expected. Interestingly, the isopycnals are displaced more than 30 m during the time series, accompanied by a clear vertical shift in the horizontal current. A similar displacement is not observed along the northern coast (TS5), which along with the observations at TS3 suggest the presence of an internal Kelvin wave propagating in-fjord from Akseløya along the southern coast, and dissipating before returning outward along the northern side. The role of Mariasundet in this process is difficult to assess. We will look more into the

process of two sounds in the numerical analysis below. We end the time series discussion by noting the main outflow along TS5, and the dominant inflow at TS6. This is in accordance with *Bergh* [2004] discussing the mean circulation in Van Mijenfjorden induced by the tidal forcing.

4. Numerical simulations, test in a box

We now proceed to study our internal wave problem numerically. As is shown in the previous section, the hydrography of Van Mijenfjorden varies considerably on short time scales. Performing a realistic simulation of the entire fjord system requires detailed information on local winds, freshwater runoff and detailed initial and boundary conditions on hydrography and currents. In this study we want to focus on the generation and propagation of internal waves. Thus, it is instructive to idealize the problem.

The model utilized is the MITgcm model [*Marshall et al.*, 1997; *Adcroft et al.*, 2004]. This is a finite volume, non-linear z-coordinate model with non-hydrostatic capabilities. The model has been widely used for study of internal waves [*Legg and Adcroft*, 2003; *Vasiliy Vlasenko and Stashchuk*, 2007; *Xing and Davies*, 2007; *Boegman and Dorostkar*, 2011]. We made preliminary attempts with ROMS [*Shchepetkin and McWilliams*, 2005], a terrain-following σ-coordinate model. However, due to the combination of stratification and steep topography, we quickly encountered problems with numerical pressure gradients [e.g. *Berntsen*, 2002]. Bottom topography in MITgcm is represented by use of shaved cells [*Adcroft et al.*, 1997]. For our model setup we apply small constant values for the horizontal and vertical diffusivity, and take for the vertical turbulent viscosity that $A_z = 0.001$ m^2 s^{-1}. The horizontal viscosity is of Smagorinsky type with value 2.2 along with a small biharmonic viscosity as suggested by *Griffies and Hallberg* [2000]. No-slip conditions are employed at side walls, along with a quadratic bottom drag coefficient of 0.0025. The time step used is 5 s, the horizontal grid size is 100 m, and we employ 32 nonuniformly spaced vertical levels with highest resolution where the

density gradient is largest. We let the model run hydrostatically, as the grid should be too coarse for non-hydrostatic effects to be observable [*Berntsen et al.*, 2009].

In our simulations we ignore the effect of wind and freshwater runoff. Initially, the system is at rest, with horizontally constant hydrography. We will later consider the Van Mijenfjorden topography, but in this section we simplify to a semi-enclosed box; see Figure 5. We denote the long side as west-east, and the short side as south-north for reference. The western boundary is open, all other boundaries are closed. At 20 km in-fjord we place a constriction resembling Akseløya. In this simplified setup we only consider one sound (Van Mijenfjorden has two), and place it on the southern side in order to avoid the complicating factor of the wave making a 90° turn in the southwestern corner. The sound depth is 20 m and width 1300 m, giving a cross sectional area similar to Akselsundet. The sloping bottom near the eastern coast is introduced as a crude wave damper to minimize reflections. The open boundary condition is on the form $u = u_0 \sin(\omega t)$, where u_0 is constant across the open boundary and $\omega = 1.4 \times 10^{-4}$ s^{-1} corresponds to the M_2 semidiurnal tide. The interior solution is relaxed toward the boundary via a 64 grid point wide sponge layer. The model is run for 48 hours, where the forcing amplitude is $u_0 / 2$ the first 6 hours to ensure smooth spin-up.

The solution will be very dependent on the choice of forcing amplitude u_0 and the vertical hydrography profile. In the following we use our idealized setup to test the response in the system when varying these parameters.

Box run 1: Van Mijen hydrography

In the first test we set forcing and hydrography to resemble the conditions in Van Mijenfjorden. From Figure 2 we want surface tidal amplitudes close to 0.5 m. If we integrate over the domain this leads approximately to a boundary forcing of $u_0 = 3$ cm s^{-1} (verified a posteriori). Regarding the hydrography, we neglect the effect of horizontal variation, and

consider only the outer part of the fjord. The profile is thus an average of the CTD-measurements from the time series stations TS2-TS5, and the sections A and C; see Figure 6.

In order to visualize the horizontal distribution of isopycnal displacements, we introduce a perturbation potential energy per unit area, defined as

$$\Delta PE(t) = PE(t) - PE_0 = \int_{-H}^{\eta(t)} \rho(t) g z dz - \int_{-H}^{0} \rho(t=0) g z dz \,. \qquad (2)$$

From this definition *PE* is negative, so a positive ΔPE indicates a mean depression in the water column. Plot of normalized ΔPE after 41 hours simulation is shown in Figure 7. The region plotted is from 20 to 45 km in-fjord, the sound is in the southwestern corner and the eastmost region with the sloping bottom is omitted. We clearly see that the most energetic displacements occur near the boundaries. These displacements propagate cyclonically around the basin similar to internal Kelvin waves. The radius of the displacement signal is 2-3 km, and when comparing similar plots from different times we obtain a propagation velocity of 40-45 cm s^{-1} (not shown). A similar velocity is obtained by considering a wavelength $\lambda = 19$ km from Figure 7 and the wave period $T_{M2} = 12.42$ hours; $\lambda / T_{M2} = 42$ cm s^{-1}.

In addition to the internal Kelvin wave signal, a second feature is evident in Figure 7. In front of the coastal wave, there is a narrow pulse which propagates radially into the basin in all directions from the sound. The velocity of the pulse is similar to that of the coastal wave, as is indicated by the circular shape. From a vertical section of density near the southern wall (Figure 8) we see more clearly the steep front of the depression, coinciding with the pulse. The vertical displacement reaches more than 20 m over 600 m horizontal distance. In the basin interior, a similar section at 5 km north (Figure 9) shows the pulse as a small train of waves which is also visible in Figure 7. We will discuss this pulse more thoroughly in section 6.

We now turn our attention to the velocities through the sound. A vertical cross section of maximum velocity u_s across the sound is presented in Figure 10. During inflow the current

peaks at 1.55 m s^{-1} in a jet around 16 m depth. The outflow is more homogenous across the sound, peaking at -1.29 m s^{-1}. This asymmetry is in accordance with tidal choking theory [*Stigebrandt*, 1980], and is thus expected. Following the discussion in section 2, we compare u_s to the baroclinic phase velocity found above. Taking conservative values of $u_s = 1.2$ m s^{-1} and $c_i = 0.45$ m s^{-1}, we obtain $F_D = 2.67$ indicating supercritical conditions, reinforcing the jet-type behavior shown in Figure 10.

Box run 2: Two-layer

With reasonable knowledge of expected baroclinic phase velocities (c_i) from realistic stratification, we setup a case with two-layer stratification. We want to roughly preserve the location of the pycnocline while keeping c_i. For simplicity we take temperature constant at 2°C, and two-layer salinity profile as shown in Figure 11. The resulting density is also shown, in which a small correction for pressure can be seen. c_i is calculated using the full two-layer expression [*Gill*, 1982]

$$c_i = \sqrt{\frac{\rho_2 - \rho_1}{\rho_2} g \frac{H_1 H_2}{H_1 + H_2}}, \tag{3}$$

which yields $c_i = 0.42$ m s^{-1} when inserting appropriate values from Figure 11.

Plot of ΔPE for the two-layer stratification after 41 hours simulation is shown in Figure 12. The structure is comparable to the previous case, with most of the energy near the south coast, and a similar pulse propagating into the basin. A vertical section near the south coast (Figure 13) reveals that most of the displacement occurs near the pycnocline, and a steepened structure similar to Figure 8 is clear. The velocities through the sound (not shown) are very similar to the previous case in structure, the maximum values are 1.52 and -1.29 m s^{-1}.

Box run 3: Test forcing

In the next set of tests we consider the sub-critical scenario by reducing the forcing. We perform two runs using the two-layer hydrography from box run 2, taking u_0 to be 0.45 cm s^{-1} and 0.9 cm s^{-1}, or 15% (*a*) and 30% (*b*) of the original forcing, respectively. ΔPE for the two runs are presented in Figure 14. We clearly see the difference between the two cases; at case *a* the pulse is almost not visible and the shape is quite similar to what we expect from a Kelvin wave (i.e. eq. (1)). At case *b* however, the pulse is more visible, and the shape is skewed more towards what we found in the box run 2.

The velocities through the sound have maximum values at -0.24 and 0.28 m s^{-1} for case *a*, and -0.45 and 0.56 m s^{-1} for case *b*. The velocity structure across the sound in the latter case is similar to box run 2 with a jet inwards and more barotropic outwards. The jet is not as visible in case *a* however; here the structure is rather similar for in- and outflow, more in accordance with subcritical conditions. Recalling that $c_i = 0.42$ m s^{-1} for this stratification, the largest Froude numbers are $F_D = 0.67$ and $F_D = 1.33$ for case *a* and case *b*, respectively.

5. Moving to realistic topography, comparison with measurements

Having obtained some experience with idealized model runs, we now apply a topography similar to Van Mijenfjorden. As this fjord has two sounds, it is interesting to isolate the effect of each sound. We also want to look into the realistic hydrography in comparison with the two-layer structure we applied in section 4.

We set up four model runs with different topography and initial hydrography; see Table 2. The bottom topography matrix is shown in Figure 15. The leftmost part is the FRS-zone, and the rightmost part of Van Mijenfjorden is omitted from the simulation. As our point of interest is close to Akseløya this should not influence our solution significantly. When a sound is closed, we simply set the depth to zero in a three-gridpoint wide band across the respective sound.

Model parameters are similar to what is used in section 4. Due to the varying depth, ΔPE (eq. (2)) is not easily visualized; instead contours of constant density are shown.

Results from the first run with realistic hydrography and topography (VMrun1) are shown in Figure 16 after 45 hours simulation. The left column shows density at three different depths. As before, we identify the internal Kelvin wave pattern along the southern coast. It is quite visible in all three depths, but most pronounced at -16.9 m. From the right column of Figure 16 it seems that the primary internal wave generation occurs at Akselsundet. We also note the pulse in all depths. Current magnitude and direction at -16.9 m depth are shown in Figure 17 at time of max inflow through Akselsundet (upper figure) and max outflow (lower figure). We see the wave along the southern coast propagating inward at all times through the tidal cycle. Near Akselsundet during inflow the current has a dominantly south eastern direction along Akseløya. During outflow the current is toward the sound from a much wider region, in accordance with tidal choking theory discussed above. Current amplitudes through Akselsundet reach 1.4-1.6 m s^{-1}.

As a means of comparing the realistic model run with the measurements, we plot model density and along-coastal current at the time series locations TS4 and TS5 (Figure 18). For the southern station (left figure), the largest currents coincide with depression of the isopycnals (low density values) in the upper layer, which agrees with Figure 16 and Figure 17. We also see a local current maximum around -60 m depth along with elevation of the isopycnals. This is also observed in the measurements (Figure 4 d). The current magnitude and the maximum isopycnal displacement are lower than what was measured. At the northern station TS5 (right figure) we see only small oscillations. The mean westward flow in the upper layer from the measurements (Figure 4 e) is not present in the model.

The next two model runs are presented in Figure 19. Here we experiment with closing Mariasundet (left column) and Akselsundet (right column) separately. The result for the left

column is quite similar to what was found in the first run (Figure 16), which should point to Akselsundet being the dominant generator for internal waves. However, as we see in the right column, closing off Akselsundet reveals a significant contribution from Mariasundet. Comparing the two columns we see that waves from Mariasundet are somewhat ahead of those from Akselsundet, but not by much. Thus the full picture in VMrun1 is close to a superposition of two internal Kelvin waves. Regarding the pulse we note that it is clearly visible in all the plotted depths, propagating radially from each respective sound.

As a last test we apply the two-layer hydrography (VMrun4), result shown in Figure 20 for -16.9 m depth. Again, a Kelvin-type signal is identifiable, along with several pulses. At -10.3 m and -28 m only slight density changes are visible (not shown).

6. Discussion and concluding remarks

Through a series of simulations and measurements we have shown strong indications of tidally induced internal wave motion in Van Mijenfjorden, an Arctic fjord in Svalbard. As expected, a major part of the internal wave energy is in the form of an internal Kelvin wave, propagating cyclonically around the fjord. Numerical tests from two-layer hydrography show that the propagating internal wave emerges whether conditions are baroclinically sub- or supercritical through the sound, as we expected from the discussion in section 2. From vertical profiles we show that the isopycnal displacements occur in regions of large vertical density gradients.

The two sounds in Van Mijenfjorden each serve as internal wave generators, though the dominant waves propagate from Akselsundet. According to the model results, a somewhat realistic hydrography gives waves that are nearly in phase from the two sounds. As propagation velocity is directly affected by the stratification, there could easily be times when the waves are perfectly in phase, as the hydrography in Van Mijenfjorden varies considerably. Thus it could be difficult to measure directly the waves from each sound. It is important to note that Mariasundet is rather small (0.7 km wide) compared to the grid size (100 m), and the representation of this sound in the topography matrix is coarse. Thus we cannot determine realistically how large the waves from this sound actually are without applying higher resolution and more accurate representation of the topography.

One must take care when directly comparing the measurement data to the model results, due to our many and crude assumptions. Firstly, we neglected wind. Thus, the modeled near surface turbulence distribution and currents are bound to differ from the measured data. Another important aspect of the wind is that it may itself set up internal waves when changing direction, as mentioned in section 2. Looking at wind data (Figure 2) we see that the wind direction in Van Mijenfjorden is unidirectional for large periods of time, which sets up a tilting interface that when released (wind changes), will propagate along the coast as an internal Kelvin wave. A

second aspect is that our model is started from rest and is run for 48 hours in an attempt to isolate the effect of internal wave propagation on an otherwise undisturbed system. In order for a mean circulation pattern to be set up, one would need a spin-up time of several days, possibly months. Thus the observed mean currents in Figure 4 e) are not observable in the model.

The wave pulse observed in the model results demands some discussion. During near super-critical conditions, a wave pulse propagates inwards from the fjord entrance at each inflow phase of the tidal cycle. This pulse is seemingly not affected by rotation, and propagates with approximately the same speed as the internal Kelvin wave. One would expect this to be some kind of KdV solitary wave [*Helfrich and Melville*, 2006]. Our simulations are nonlinear but do not include the non-hydrostatic term, and are thus in violation of the non-hydrostatic requirements of the KdV solution. *Horn et al.* [1999] discusses this very problem in hydrostatic models. They explain that the initial evolution and steepening of the wave may be explained by the nonlinear hydrostatic wave equation [*Long*, 1972]:

$$\xi_t + c_i \xi_x + \alpha \xi \xi_x = 0, \tag{4}$$

where α is a nonlinear coefficient. After the development of the front, viscosity enters the equation as a balancing term. The resulting wave front propagates as a balance between nonlinear steepening and viscosity. This is probably what we see in our simulations. We should at this point note that we did a test with non-hydrostatic dynamics turned on. This yielded little difference in the results, probably due to insufficient horizontal resolution. Regarding generation of the pulse, it is not surprising that we do not observe the pulse during weak forcing events. When flow through the sound is laminar, we expect the linear solution to be dominant. More abrupt vertical motion associated with stronger forcing is what sets off the nonlinear wave.

Acknowledgements

The author is greatly indebted to Prof. Ilker Fer at Univ. of Bergen for the opportunity to join the cruise in Van Mijenfjorden and gain access to the data presented in this paper. He is also grateful to Prof. Jarle Berntsen and Dr. Jiuxing Xing for valuable input on the model configuration.

Adcroft, A., C. Hill, and J. Marshall (1997), Representation of Topography by Shaved Cells in a Height Coordinate Ocean Model, *Mon. Weather Rev.*, *125*(9), 2293-2315.

Adcroft, A., C. Hill, J.-M. Campin, J. Marshall, and P. Heimbach (2004), Overview of the formulation and numerics of the MITgcm, in *Proceedings of the ECMWF seminar series on Numerical Methods, Recent developments in numerical methods for atmosphere and ocean modelling*, pp. 139-149, ECMWF.

Bergh, J. (2004), Measured and modelled tidally driven mean circulation under ice cover in Van Mijenfjorden, Master thesis, 65 pp, Gothenburg, Gothenburg University.

Berntsen, J. (2002), Internal Pressure Errors in Sigma-Coordinate Ocean Models, *J. Atmos. Oceanic Technol.*, *19*(9), 1403-1414.

Berntsen, J., J. Xing, and A. Davies (2009), Numerical studies of flow over a sill: sensitivity of the non-hydrostatic effects to the grid size, *Ocean Dynamics*, *59*(6), 1043-1059.

Boegman, L., and A. Dorostkar (2011), Three-dimensional simulation of NLIW generation, propagation and breaking in Cayuga Lake, in *7th Int. Symp. on Stratified Flows*, edited, Rome, Italy.

Brown, P. J. (1973), Kelvin-wave reflection in a semi-infinite canal, *J. Mar. Res.*, *31*(1), 1-10.

Cottier, F. R., F. Nilsen, R. Skogseth, V. Tverberg, J. Skarðhamar, and H. Svendsen (2010), Arctic fjords: a review of the oceanographic environment and dominant physical processes, *Geological Society, London, Special Publications*, *344*(1), 35-50.

Farmer, D. M., and H. J. Freeland (1983), The Physical Oceanography of Fjords, *Prog. Oceanogr.*, *12*(2), 147-220.

Fer, I., and K. Widell (2007), Early spring turbulent mixing in an ice-covered Arctic fjord during transition to melting, *Cont. Shelf Res.*, *27*, 1980-1999.

Fer, I., R. Skogseth, and F. Geyer (2010), Internal Waves and Mixing in the Marginal Ice Zone near the Yermak Plateau*, *J. Phys. Oceanogr.*, *40*(7), 1613-1630.

Gill, A. E. (1982), *Atmosphere-Ocean Dynamics*, Academic Press.

Griffies, S. M., and R. W. Hallberg (2000), Biharmonic Friction with a Smagorinsky-Like Viscosity for Use in Large-Scale Eddy-Permitting Ocean Models, *Mon. Weather Rev.*, *128*(8), 2935-2946.

Helfrich, K. R., and W. K. Melville (2006), Long Nonlinear Internal Waves, *Annual Review of Fluid Mechanics*, *38*, 395.

Horn, D., J. Imberger, and G. Ivey (1999), Internal solitary waves in lakes—a closure problem for hydrostatic models, in, 11th 'Aha Huliko'a Hawaiian Winter Workshop, University of Hawaii.

Inall, M., F. Cottier, C. Griffiths, and T. Rippeth (2004), Sill dynamics and energy transformation in a jet fjord, *Ocean Dynamics*, *54*, 307-314.

Legg, S., and A. Adcroft (2003), Internal Wave Breaking at Concave and Convex Continental Slopes*, *J. Phys. Oceanogr.*, *33*(11), 2224-2246.

Llewellyn Smith, S. G. (2004), Stratified rotating edge waves, *J. Fluid Mech.*, *498*, 161-170.

Long, R. R. (1972), The steepening of long, internal waves, *Tellus*, *24*(2), 88-99.

Marchenko, A. V., E. G. Morozov, S. V. Muzylev, and A. S. Shestov (2010), Interaction of Short Internal Waves with the Ice Cover in an Arctic Fjord, *Oceanology*, *50*(1), 18-27.

Marshall, J., A. Adcroft, C. Hill, L. Perelman, and C. Heisey (1997), A finite-volume, incompressible Navier Stokes model for studies of the ocean on parallel computers, *J. Geophys. Res.*, *102*(C3), 5753-5766.

Morozov, E. G., and A. V. Marchenko (2012), Short-period internal waves in an arctic Fjord (Spitsbergen), *Izv. Atmos. Ocean. Phys.*, *48*(4), 401-408.

Padman, L., and T. M. Dillon (1991), Turbulent Mixing Near the Yermak Plateau During the Coordinated Eastern Arctic Experiment, *J. Geophys. Res.*, *96*(C3), 4769-4782.

Padman, L., and S. Erofeeva (2004), A barotropic inverse tidal model for the Arctic Ocean, *Geophys. Res. Lett.*, *31*.

Rainville, L., and R. A. Woodgate (2009), Observations of internal wave generation in the seasonally ice-free Arctic, *Geophys. Res. Lett.*, *36*(23), L23604.

Shchepetkin, A. F., and J. C. McWilliams (2005), The regional oceanic modeling system (ROMS): a split-explicit, free-surface, topography-following-coordinate oceanic model, *Ocean Modelling*, *9*(4), 347-404.

Skarðhamar, J., and H. Svendsen (2010), Short-term hydrographic variability in a stratified Arctic fjord, *Geological Society, London, Special Publications*, *344*(1), 51-60.

Stashchuk, N., M. Inall, and V. Vlasenko (2007), Analysis of Supercritical Stratified Tidal Flow in a Scottish Fjord, *J. Phys. Oceanogr.*, *37*(7), 1793-1810.

Stigebrandt, A. (1980), Some Aspects of Tidal Interaction with Fjord Constrictions, *Estuarine and Coastal Marine Science*, *11*(2), 151-166.

Stigebrandt, A., and J. Aure (1989), Vertical Mixing in Basin Waters of Fjords, *J. Phys. Oceanogr.*, *19*(7), 917-926.

Støylen, E., and J. E. H. Weber (2010), Mass transport induced by internal Kelvin waves beneath shore-fast ice, *J. Geophys. Res.*, *115*(C3), C03022.

Svendsen, H., et al. (2002), The physical environment of Kongsfjorden–Krossfjorden, an Arctic fjord system in Svalbard, *Pol. Res.*, *21*(1), 133-166.

Vlasenko, V., and N. Stashchuk (2007), Three-dimensional shoaling of large-amplitude internal waves, *J. Geophys. Res.*, *112*(C11), C11018.

Vlasenko, V., N. Stashchuk, K. Hutter, and K. Sabinin (2003), Nonlinear internal waves forced by tides near the critical latitude, *Deep Sea Res., Part I*, *50*(3), 317-338.

Weber, J. E. H., and E. Støylen (2011), Mean drift velocity in the Stokes interfacial edge wave, *J. Geophys. Res.*, *116*(C4), 8.

Widell, K., I. Fer, and P. M. Haugan (2006), Salt release from warming sea ice, *Geophys. Res. Lett.*, *33*(12), L12501.

Xing, J., and A. M. Davies (2007), On the importance of non-hydrostatic processes in determining tidally induced mixing in sill regions, *Cont. Shelf Res.*, *27*(16), 2162-2185.

Name	B1	A1	C1	TS1	TS2	C2	TS3
Time	0920-1000	1002-1004	1006-1009	1010-1023	1100-1113	1113-1116	1117-1206
No. of samples	10	10	11	18	27	11	27
Depth	42-87	61-117	41-110	60	60	42-114	84

Name	TS4	A2	TS5	A3	B2	TS6	D
Time	1207-1220	1220-1223	1223-1312	1312-1315	1317-1319	1320-1409	1409-1415
No. of samples	27	10	27	10	11	27	15
Depth	79	31-112	79	32-113	34-88	66	33-113

Table 1: CTD collection data. Names A-D denote horizontal sections, TS1-TS6 time series. A1-A3, B1-B2, C1-C2 are repeated sections. Time is date of August, and hour [DDHH]. Depth [m] is min-max for sections, average for time series.

	VMrun1	VMrun2	VMrun3	VMrun4
Topography:	Realistic	Mariasundet closed	Akselsundet closed	Realistic
Hydrography:	Realistic	Realistic	Realistic	Two-layer

Table 2: Setup of the four Van Mijenfjorden model runs.

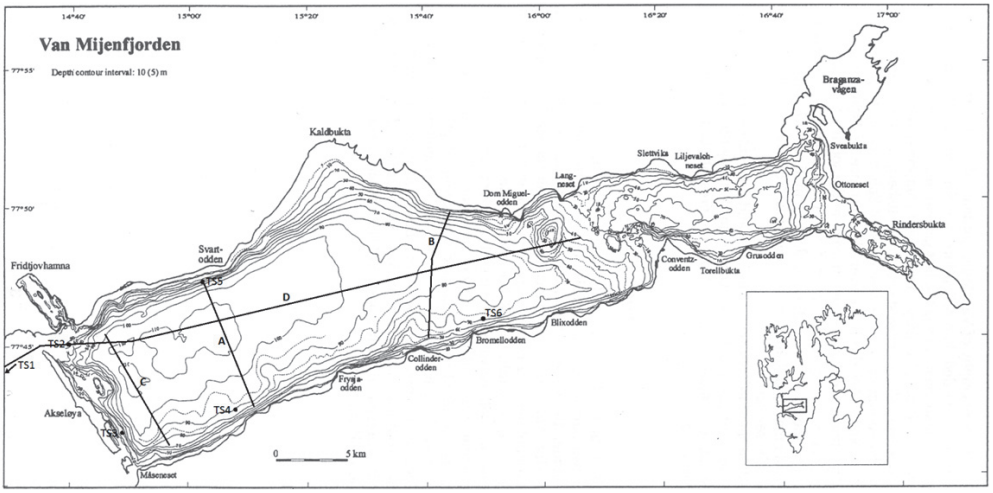

437

438 Figure 1: Map of Van Mijenfjorden in Svalbard, situated at 77.8°N, 15.5°E [*Bergh*, 2004]. Lines

439 and dots denote CTD measurement sections and time series stations (Table 1).

440

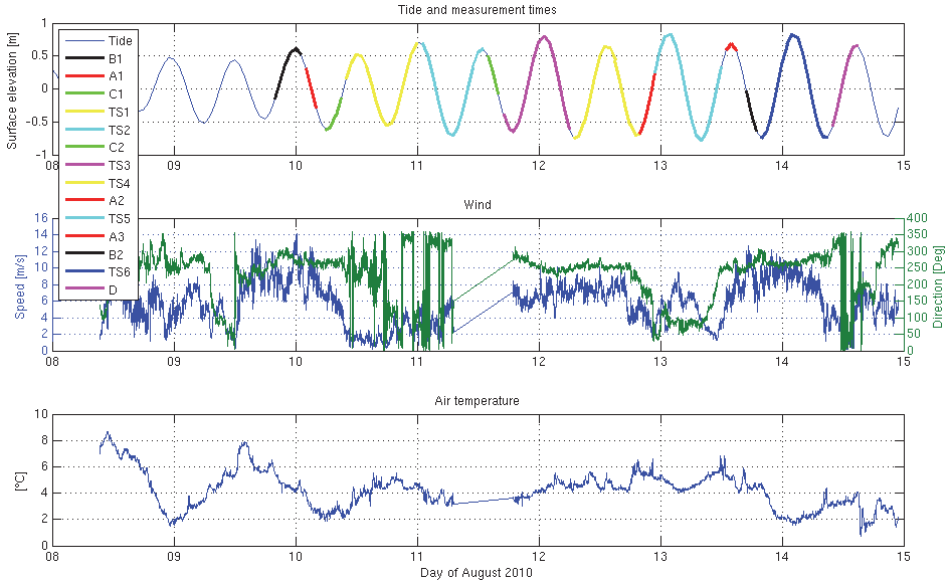

441

442 Figure 2: *Upper:* Tidal surface amplitude outside Van Mijenfjorden from the AOTIM-5 model

443 [*Padman and Erofeeva*, 2004]. Colored overlay represents time of measurements. *Middle and*

444 *lower:* Wind direction and speed, and air temperature, measured on RV *Håkon Mosby*. Data was

445 not recorded in the period 0715-1851 the 11th.

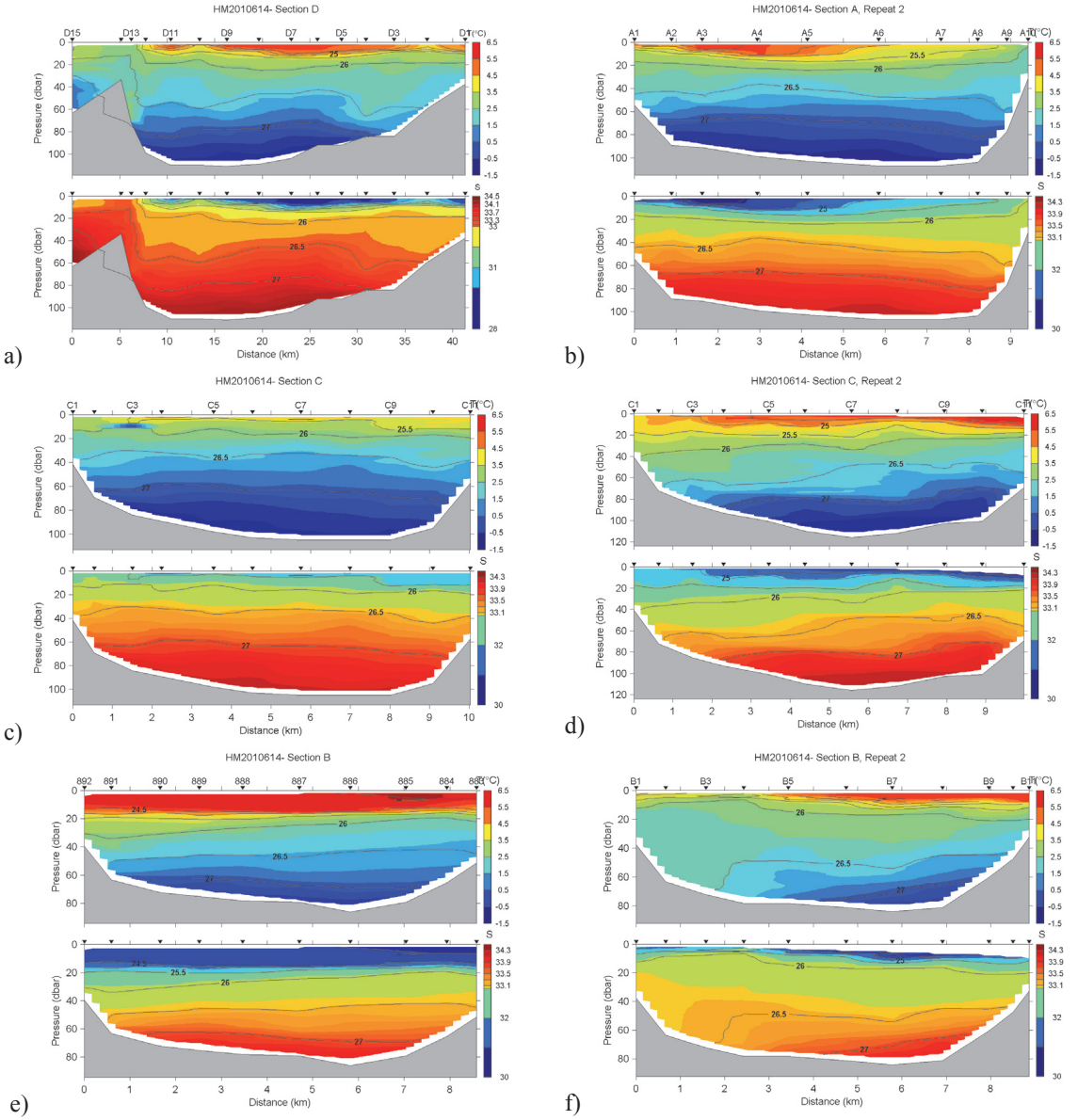

Figure 3: Temperature and salinity (color) and density (black contours) for CTD sections a) D, b) A2, c) C1, d) C2, e) B1 and f) B2. Orientation of the figures are west-east in a), and south-north in b)-f). See Figure 1 and Table 1 for reference.

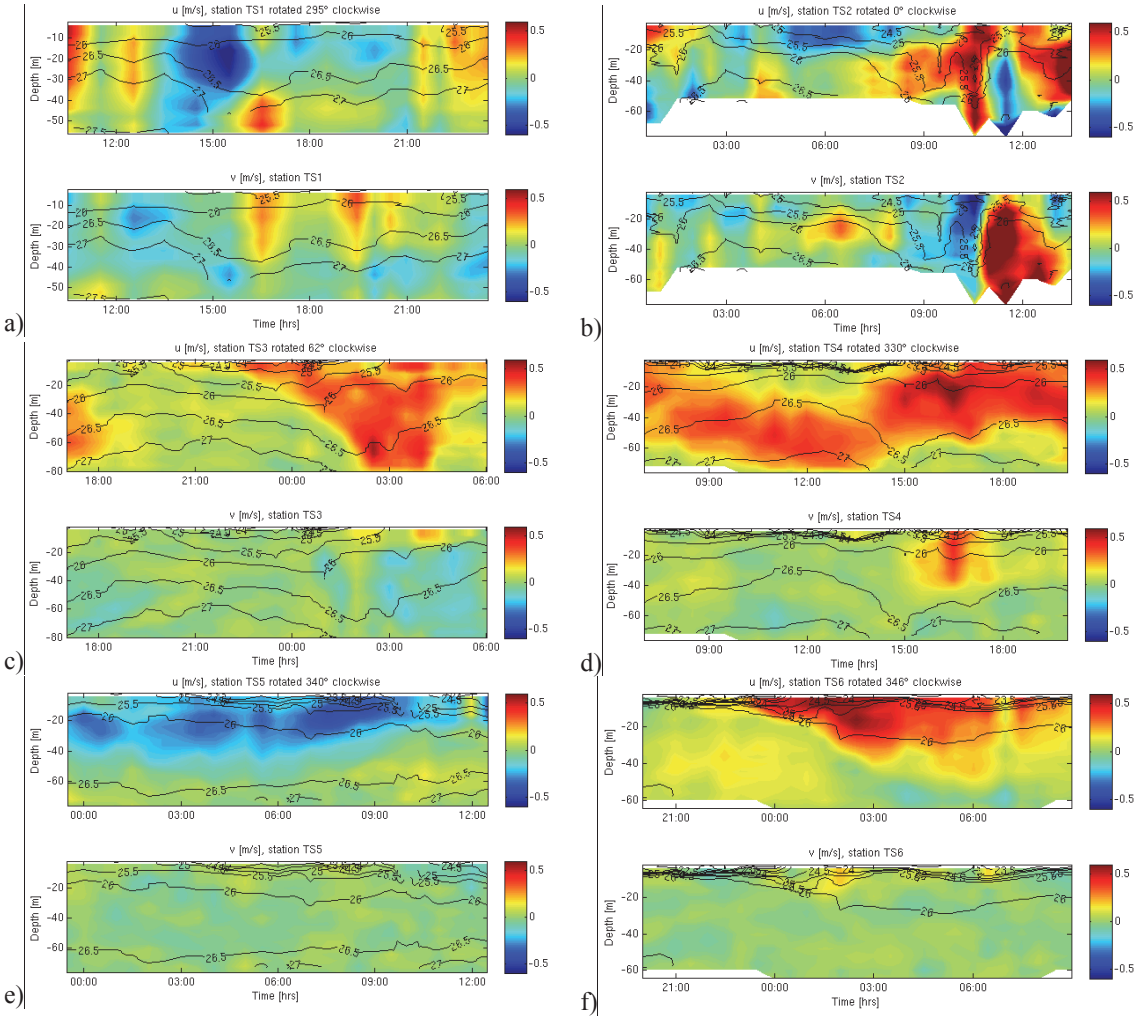

452 Figure 4: u and v velocities (color) and density (σ_t, black contours) for each time series station.

453 a)-f) correspond to TS1-TS6 respectively. Axis are rotated so u is aligned eastward along the

454 coast where applicable (TS3-TS6), or along a direct line inwards through Akselsundet (TS1-

455 TS2).

456

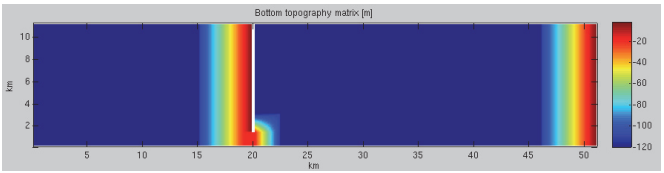

457

Figure 5: Bottom topography test box run. The western boundary is the only open boundary.

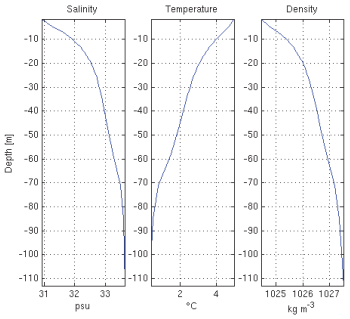

Figure 6: Initial hydrography for box run 1.

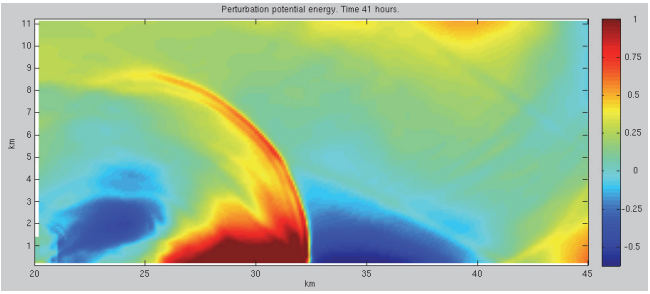

Figure 7: Horizontal plot of normalized perturbation potential energy ΔPE after 41 hours, box run 1. The plotted region corresponds to the first 25 km of the inner basin, see Figure 5. Red and blue indicate depression and elevation respectively, see Figure 8.

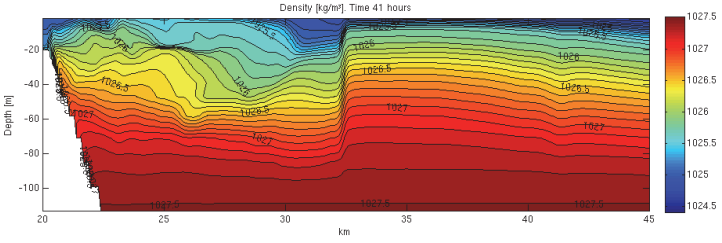

Figure 8: Vertical section of density near southern coast between 20 and 45 km east after 41 hours simulation, box run 1. Contour interval is 0.1 kg m^{-3}.

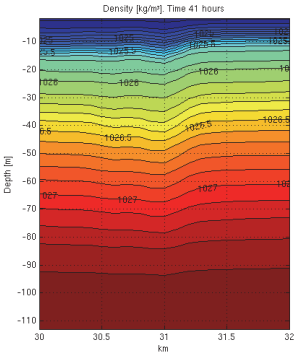

Figure 9: Section of density after 41 hours similar to Figure 8. Section taken at 5 km north, 30-32 km east.

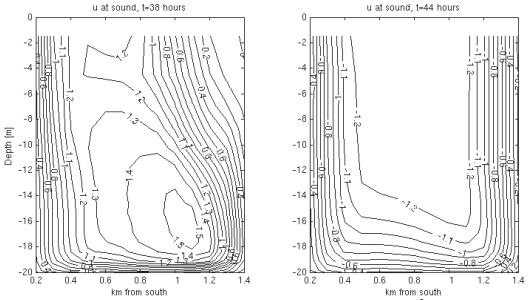

Figure 10: Cross-sectional velocity [m s^{-1}] at time of maximum inflow (left) and outflow (right) through the sound at 20 km east for box run 1. Left-right on the figures correspond to south-north.

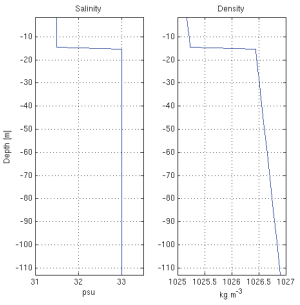

Figure 11: Initial hydrography for box run 2. Temperature is constant at 2°C and not shown.

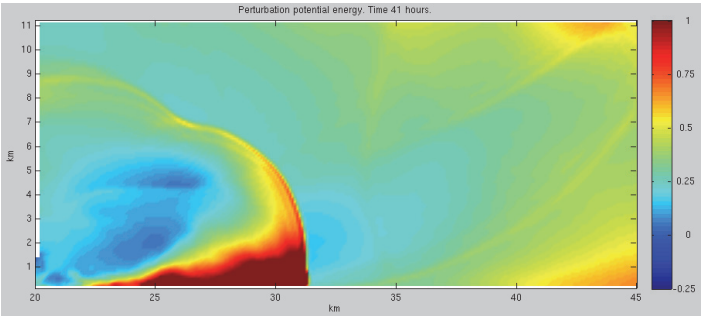

Figure 12: Normalized ΔPE (similar to Figure 7) after 41 hours simulation, box run 2.

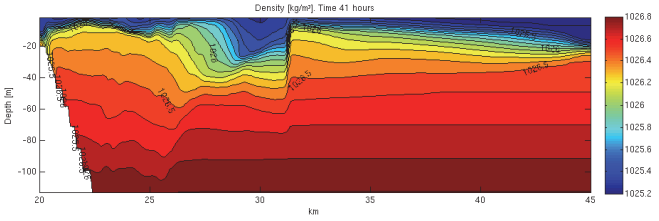

Figure 13: Vertical section of density near southern coast after 41 hours simulation, box run 2. Contour interval is 0.1 kg m^{-3}.

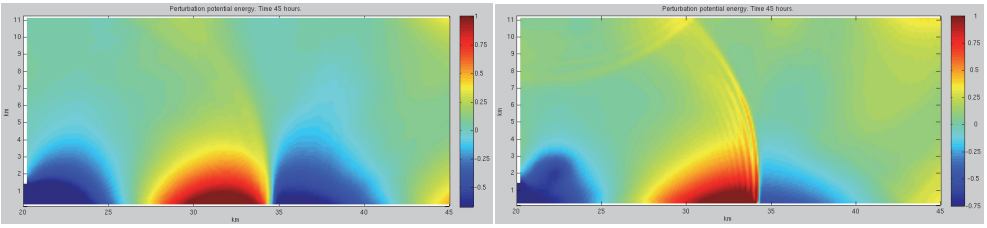

Figure 14: Normalized ΔPE (similar to Figure 7) after 45 hours simulation, box runs 3. Forcing at 15% (*Left, case a*) and 30% (*Right, case b*) of original forcing.

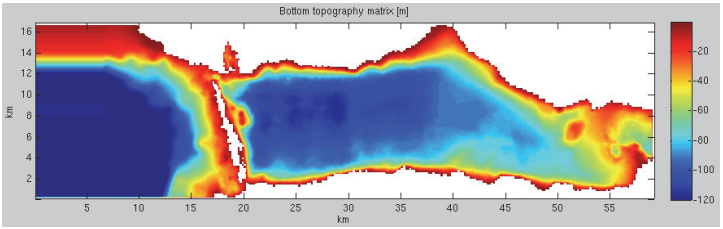

Figure 15: Bottom topography Van Mijenfjorden.

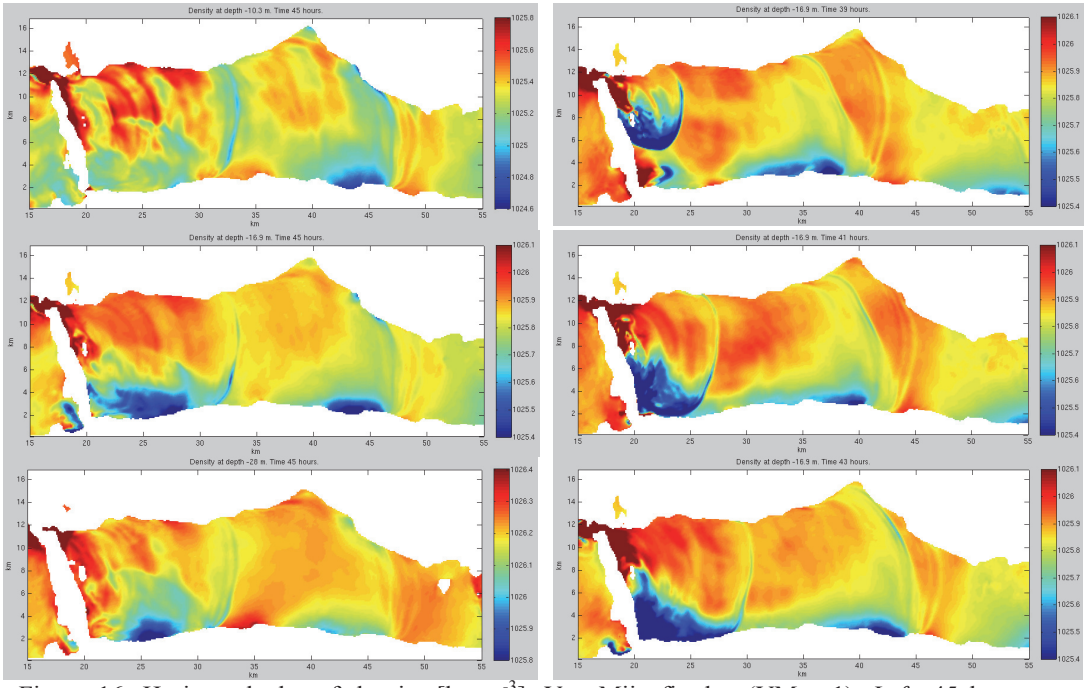

Figure 16: Horizontal plot of density [kg m^{-3}], Van Mijenfjorden (VMrun1). *Left:* 45 hours simulated; depth 10.3 m (*upper*), 16.9 m (*middle*), 28 m (*lower*). *Right:* Depth 16.9 m; 39 hours (*upper*), 41 hours (*middle*), 43 hours (*lower*).

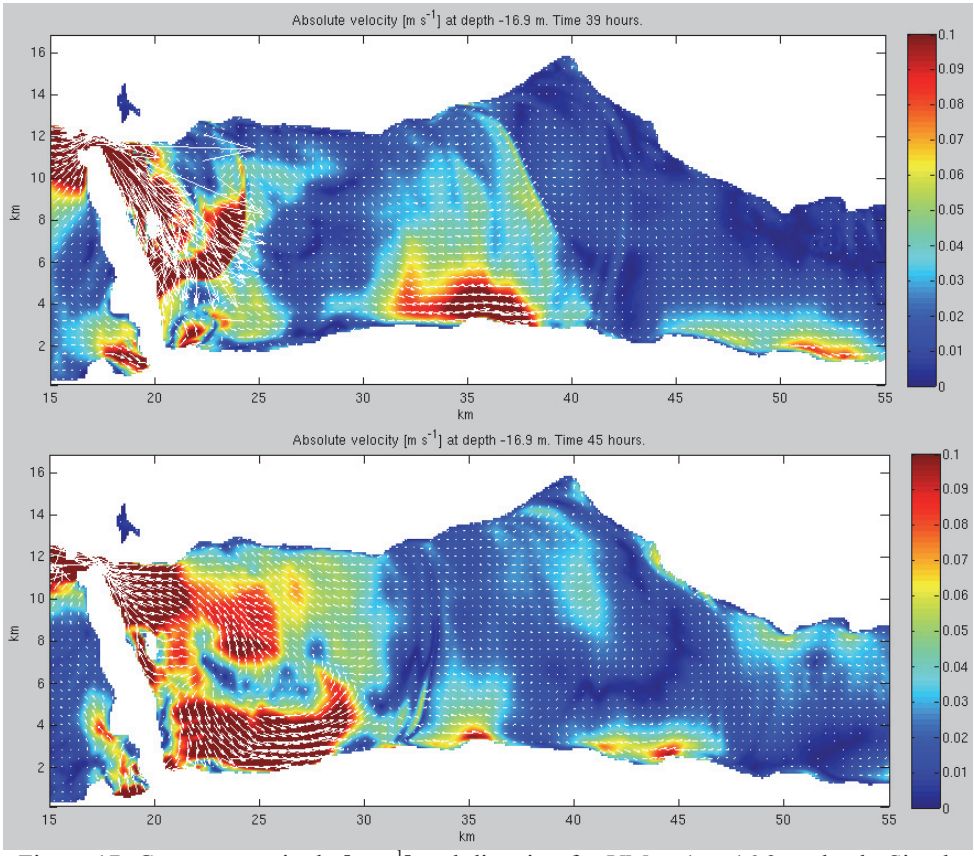

503 Figure 17: Current magnitude [m s^{-1}] and direction for VMrun1 at 16.9 m depth. Simulated 39

504 hours (*upper*) and 45 hours (*lower*).

505

506

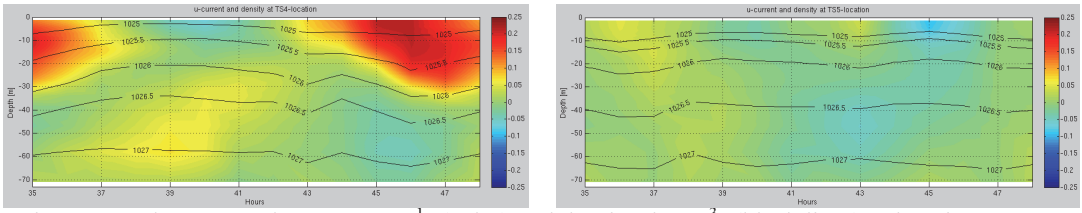

507 Figure 18: Along-coastal current [m s^{-1}] (color) and density [kg m^{-3}] (black lines) at location TS4

508 (*left*) and TS5 (*right*) from VMrun1, 35-48 hours simulated.

509

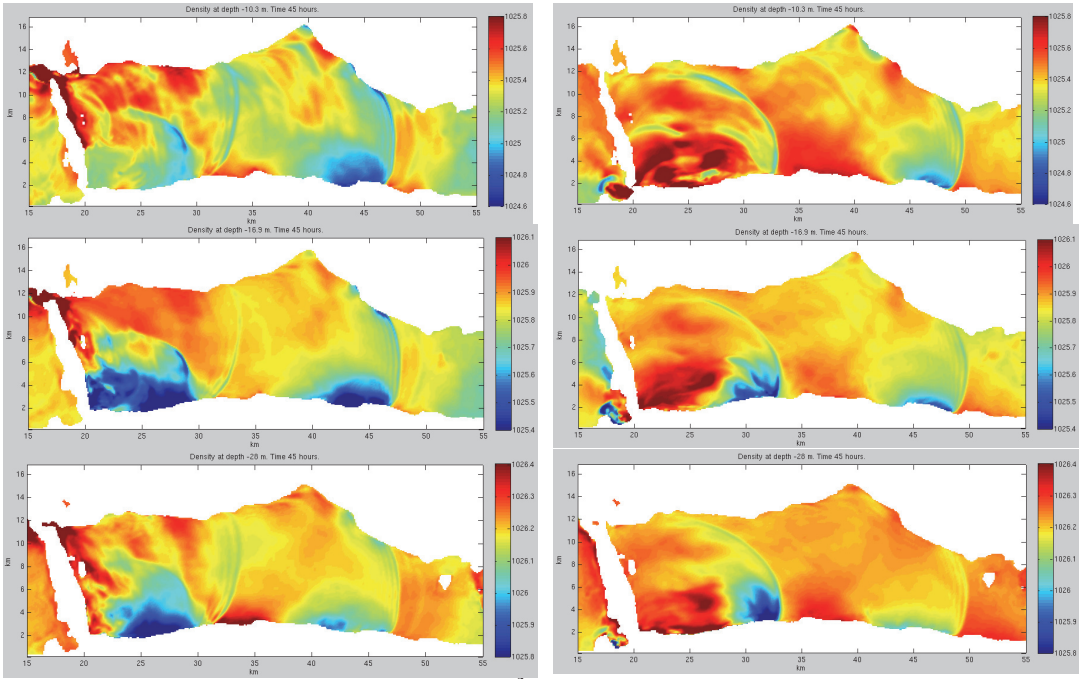

510 Figure 19: Horizontal plot of density [kg m^{-3}]. *Left:* Mariasundet closed (VMrun2). *Right:*

511 Akselsundet closed (VMrun3). *Upper*: 10.3 m, *middle:* 16.9 m, *lower:* 28 m.

512

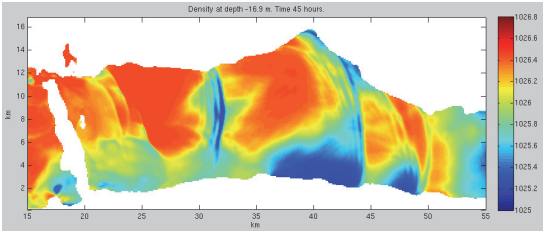

513

514 Figure 20: Horizontal plot of density [kg m^{-3}] after 45 hours simulation, 16.9 m depth. Two-layer

515 hydrography profile (VMrun4).

516

517

518